

Cell Detection by Functional Inverse Diffusion and Non-negative Group Sparsity—Part I: Modeling and Inverse Problems

Pol del Aguila Pla, *Student Member, IEEE*, and Joakim Jaldén, *Senior Member, IEEE*

Abstract—In this two-part paper, we present a novel framework and methodology to analyze data from certain image-based biochemical assays, e.g., ELISPOT and Fluorospot assays. In this first part, we start by presenting a physical partial differential equations (PDE) model up to image acquisition for these biochemical assays. Then, we use the PDEs' Green function to derive a novel parametrization of the acquired images. This parametrization allows us to propose a functional optimization problem to address inverse diffusion. In particular, we propose a non-negative group-sparsity regularized optimization problem with the goal of localizing and characterizing the biological cells involved in the said assays. We continue by proposing a suitable discretization scheme that enables both the generation of synthetic data and implementable algorithms to address inverse diffusion. We end Part I by providing a preliminary comparison between the results of our methodology and an expert human labeler on real data. Part II is devoted to providing an accelerated proximal gradient algorithm to solve the proposed problem and to the empirical validation of our methodology.

Index Terms—Inverse problems, Biomedical imaging, Convex optimization, Source localization, Biological modeling

I. INTRODUCTION

BIOLGICAL processes in which cells generate particles that diffuse in a solution and bind to receptors are ubiquitous [1]–[6]. Such processes are often measured using biochemical assays where cells are contained in a well with a receptor-coated bottom, and an image of the resulting density of bound particles is obtained. Examples include the ELISPOT [7] and Fluorospot [8] assays. If particles bind relatively close to their origin, the cells that generated these particles (active

cells) can be localized in the obtained image. Localization enables counting, and therefore, quantitative studies of the proportions of active cells within the cell population under study. Thereby, these assays provide answers to relevant questions in fields ranging from biochemical, pharmacological, and medical research [5], [9], [10], to the diagnosis of specific diseases [11], [12]. Hence, source localization (SL) algorithms are critical to the development of automated analysis systems for high-throughput pharmacological and medical applications. In this first part of our paper, we present a 2-dimensional (2D) equivalent diffusion model for the density of bound particles generated by a 3D reaction-diffusion-adsorption-desorption process. We then propose a functional optimization framework for inverse 2D diffusion that promotes stationary-source explanations of the observed data. Then, we present a discretization scheme that allows both for the synthesis of realistic data and for numerical solutions to the proposed optimization problem. Part II of this paper [13] is devoted to algorithmic solutions to solve this optimization problem.

The accuracy of SL algorithms becomes critical when characterizing cell sub-populations by multiplex assays, e.g. Fluorospot [8]. Multiplex assays allow different kinds of particles to be independently and simultaneously measured, yielding collocated images. The results of their analyses are then merged to detect which cells were producing which combinations of particle types. This data fusion is conducted based on the only comparable feature of multiple-secreting cells in each of the images, i.e., their location. Therefore, localization accuracy has a direct impact on the estimated proportions, i.e., on the accuracy of multiplex assays. The optimization framework we propose uses a non-parametric model-based approach to produce results that enable accurate SL and, thereby, accurate results in multiplex assays. In finalizing this first part, we provide results on real data by comparing our solution to the labeling of a human expert. In Part II of this paper [13], we provide a thorough evaluation of the proposed methodology using synthetic data.

SL on 2D or 3D data from linear observation models has been widely studied for biologic [14]–[22], astronomic [23], [24], acoustic [25], [26], heat conduction [27], [28], and environmental applications [29]–[31], as well as in more generic settings [32]–[36]. Parametric approaches to SL have been thoroughly investigated when the source-map is observed through a convolutional operator [20], [25], [33], [34]. In

Manuscript received September 21, 2017; revised March 31, 2018 and July 9, 2018; accepted August 24, 2018. Date of publication September 3, 2018; date of current version September 14, 2018. The associate editor coordinating the review of this manuscript and approving it for publication was Prof. Mark A. Davenport. This work was supported in part by Mabtech AB and in part by the Swedish Research Council (VR) under Grant 2015-04026. (*Corresponding author: Pol del Aguila Pla.*)

The authors are with the Department of Information Science and Engineering, School of Electrical Engineering and Computer Science, KTH Royal Institute of Technology, Stockholm 11428, Sweden (e-mail: poldap@kth.se; jalden@kth.se).

This paper has supplementary downloadable material available at <http://ieeexplore.ieee.org>, provided by the authors. The material includes detailed derivations of some key steps and further experimental results. This material is 533 kB in size.

Color versions of one or more of the figures in this paper are available online at <http://ieeexplore.ieee.org>.

Author's own archival version. Digital Object Identifier of the original manuscript: 10.1109/TSP.2018.2868258.

particular, sparsity-based approaches have been shown to have many favorable properties in this case (see [37] and references therein). To our knowledge, SL from data obtained from linear diffusion has only been addressed parametrically [29]–[31]. A downside of parametric approaches is that the full characterization of the observation system is seldom available and, thus, it has to be specifically measured [29] or estimated [38]. This implies additional costs for practical use, which hinder scalability. Non-parametric approaches to image-based SL can be divided in two categories. On one hand, model-independent approaches work solely on image properties, yielding heuristic methods to find dot-like shapes in images [14]–[19]. These are combined with generic data-analytic procedures to address measurement-noise and yield results that may be satisfactory, but are biased by the arbitrary heuristics and tend to over- or under-react to small perturbations. On the other hand, model-based approaches use the structure of the problem, exploiting properties specific to the process that generated the data without requiring previous measurement of the intrinsic values that regulate it. Most representative of these model-based non-parametric approaches are blind deconvolution methods, e.g., [35]. The inverse diffusion approach we present is model-based and non-parametric, providing a robust and scalable methodology to address SL in reaction-diffusion-adsorption-desorption models.

The inversion of diffusion equations has been widely studied [28], [39]–[41]. However, most methods address the ill-posedness of the problem by regularizing it to favor smooth solutions, i.e., by aiming to provide the least sharp release of particles over time and space that explains the data. In SL, however, one is assuming that the data has been created by localized sources. Consequently, one would want to favor the most localized, i.e., spatially sharpest, release of particles over time that explains the data. There are some approaches that target diffusion-based SL, or, closely related, the recovery of non-smooth solutions from inverse diffusion problems [27], [29]–[31]. However, inverse diffusion leads to very different problem formulations depending on the restrictions one imposes on the generation of particles, the boundary conditions of the medium, i.e., the additional effects one takes into account (such as adsorption and desorption), and the kind of measurements one has access to. [29]–[31] study 2D reaction-advection-diffusion, but only consider particles released from a single point, and intend to localize it as accurately as possible. This allows for a study specific to SL, in the sense that generic inversion of the diffusion equation is unnecessary. In particular, [30], [31] provide technical results on the identifiability of a single source. In contrast, [27] studies 1D diffusion with known-concentration boundary conditions, and while it allows for an initial concentration of particles that varies throughout the considered area, it does not contemplate the effect of the continuous generation of particles (reaction). In this paper, we study 3D reaction-diffusion-adsorption-desorption, we do not impose any restrictions on reaction, and we do not presume any artificial Dirac behavior in the spatial or temporal domains. Instead, we use regularization to favor explanations of the data that are spatially sparse and temporally continuous, as stationary cells releasing particles would be.

A. Notation

When sets and spaces of numbers are involved, we will use either standard notation such as $\mathbb{R}_+ = [0, +\infty)$, $\mathbb{R} = \mathbb{R} \cup \{-\infty, +\infty\}$ and $\mathbb{R}_+ = [0, +\infty]$ or capital non-Latin letters, e.g., we will use $\Omega = \mathbb{R}^2 \times \mathbb{R}_+$ because of the many times we will refer to functions in this particular support. When discussing locations in \mathbb{R}^2 , we will note them as bold face letters, e.g., $\mathbf{r} \in \mathbb{R}^2$.

When discussing functional sets and spaces, we will use capital calligraphic notation, such as \mathcal{X} for a generic normed space, which will have norm $\|\cdot\|_{\mathcal{X}}$. If \mathcal{X} is also a Hilbert space, \mathcal{X} will have scalar product $(\cdot|\cdot)_{\mathcal{X}}$. For any functional space \mathcal{X} , $\mathcal{X}_+ \subset \mathcal{X}$ is the cone of non-negative functionals. Specifically, if \mathcal{X} contains functionals $f : \mathcal{Y} \rightarrow \mathbb{R}$, then $\mathcal{X}_+ = \{f \in \mathcal{X} : f(y) \geq 0, \forall y \in \mathcal{Y}\} \subset \mathcal{X}$. For any set $\mathcal{Z} \subseteq \mathcal{X}$, its $(\infty, 0)$ -indicator function is the function $\delta_{\mathcal{Z}} : \mathcal{X} \rightarrow \{0, +\infty\}$ such that $\delta_{\mathcal{Z}}(x) = 0$ if $x \in \mathcal{Z}$ and $\delta_{\mathcal{Z}}(x) = +\infty$ if $x \in \mathcal{Z}^c = \mathcal{X} \setminus \mathcal{Z}$, while its $(0, 1)$ -indicator function is the function $i_{\mathcal{Z}} : \mathcal{X} \rightarrow \{0, 1\}$ such that $i_{\mathcal{Z}}(x) = 1$ if $x \in \mathcal{Z}$ and $i_{\mathcal{Z}}(x) = 0$ if $x \in \mathcal{Z}^c$.

When discussing a specific functional $f \in \mathcal{X}$, $f_+ : \mathcal{Y} \rightarrow \mathbb{R}$ will be its positive part, i.e., $f_+(y) = \max\{f(y), 0\}, \forall y \in \mathcal{Y}$. The support of the functional $f \in \mathcal{X}$ will be written as $\text{supp}(f) = \{y \in \mathcal{Y} : f(y) \neq 0\} \subset \mathcal{Y}$. Finally, for any two given functions $f, g : \mathbb{R}^N \rightarrow \mathbb{R}$ for some $N \in \mathbb{N}$, we refer to their convolution as $(f * g)$ and to the j -th convolutional power of f as f^{j*} .

When discussing operators, if \mathcal{Z} is some normed space, we will write $\mathcal{L}(\mathcal{X}, \mathcal{Z})$ for the space of linear continuous operators from \mathcal{X} to \mathcal{Z} . Coherently with the notation above, this space of operators will have norm $\|\cdot\|_{\mathcal{L}(\mathcal{X}, \mathcal{Z})}$. We will note operators as A or B , e.g., $B \in \mathcal{L}(\mathcal{X}, \mathcal{Z})$. For any such B , we will refer to its adjoint as $B^* \in \mathcal{L}(\mathcal{Z}, \mathcal{X})$. Recall that, if \mathcal{X} and \mathcal{Z} are Hilbert spaces, $(Bx|z)_{\mathcal{Z}} = (x|B^*z)_{\mathcal{X}}$, for any $x \in \mathcal{X}$ and any $z \in \mathcal{Z}$.

When discussing matrices and tensors, the space of real M -by- N matrices for some $M, N \in \mathbb{N}$ is $\mathbb{T}(M, N)$, while its element-wise positive cone is $\mathbb{T}_+(M, N)$. For a specific matrix $\tilde{f} \in \mathbb{T}(M, N)$, we specify it as a group of its elements $\left\{ \tilde{f}_{m,n} \right\}$ for $m \in \{1, 2, \dots, M\}$ and $n \in \{1, 2, \dots, N\}$. For tensors, we work analogously by adding appropriate indexes, e.g., $\tilde{f} \in \mathbb{T}(M, N, K)$ and $\left\{ \tilde{f}_{m,n,k} \right\}$ for $k \in \{1, 2, \dots, K\}$.

When presenting our statements, we will refer to them as properties if they are not novel, but are necessary for clear exposition, lemmas if they contain minor novel contributions and theorems if they constitute major novel contributions.

II. DATA MODEL

A. Physical model

We consider a physically motivated 3D stochastic model where cells are immobilized on a flat surface, represented here by the xy -plane. Some of these cells are active, i.e., they release particles into a medium located above the surface, in the half-space $z \geq 0$. Released particles then move in a 3D isotropic Brownian motion. The same surface where the cells reside is evenly coated with imperfect receptors

tuned specifically to the released particles. Therefore, particles diffusing in the medium that collide with the surface may bind to it, but also, bound particles may disassociate from the surface after some time. Particles bound to the surface at a time T , i.e., when the experiment finishes, are then tagged with some visible marker, and their density is imaged. This produces spots around each active cell in the captured image. The model is illustrated at a particle level in Fig. 1, which also includes a section from a typical observation from a Fluorospot assay. Note here that cells are tens of μms in diameter and that the particles of interest are typically of a few nm s in diameter [42]. Moreover, the visible spots produced by active cells in these assays are typically no more than $200 \mu\text{m}$ in diameter. Because these assays are conducted inside wells of approximately 7 mm in diameter, we disregard the effects of the borders of the well for the rest of the paper.

We assume that the medium is homogeneous and that the particle concentrations are low enough so that we can consider the binding affinity and disassociation rate of the surface constant and uniform. These assumptions imply that we can model the movement of individual particles as independent of each other, which renders the model spatially invariant in any direction on the xy -plane. These assumptions are also consistent with the models considered in, e.g., [1]–[6].

Consider the function $c : \mathbb{R}^2 \times \mathbb{R}_+ \times \mathbb{R}_+ \rightarrow \mathbb{R}_+$ such that $c(x, y, z, t)$ [m^{-3}] is the time-varying concentration of free particles in the medium. This concentration c is modeled via the 3D homogeneous diffusion equation,

$$\frac{\partial}{\partial t} c = D \Delta c, \quad (1a)$$

where $\Delta = \partial^2/\partial x^2 + \partial^2/\partial y^2 + \partial^2/\partial z^2$ is the Laplace operator and D [m^2s^{-1}] is the diffusion constant of the released particles in the medium. Consider now the function $d : \mathbb{R}^2 \times [0, +\infty) \rightarrow \mathbb{R}_+$ such that $d(x, y, t)$ [m^{-2}] is the surface density of bound particles at time t . This density d is coupled to c via the adsorption-desorption boundary condition [43], given by

$$\frac{\partial}{\partial t} d = \kappa_a c|_{z=0} - \kappa_d d, \quad (1b)$$

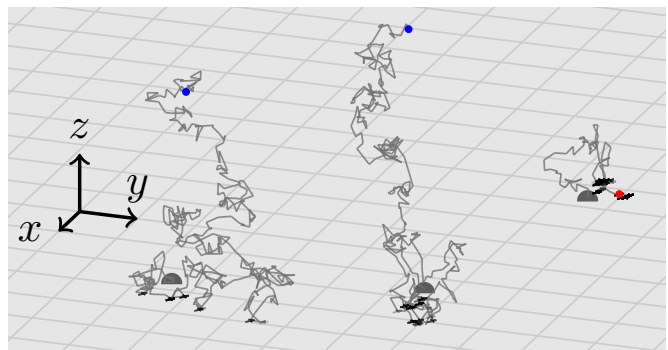
and via the condition on the flow of particles away from the surface [4], given by

$$-D \frac{\partial}{\partial z} c|_{z=0} = s + \kappa_d d - \kappa_a c|_{z=0}. \quad (1c)$$

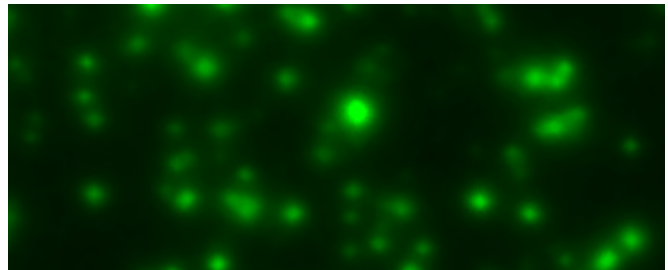
Here, the function $s : \mathbb{R}^2 \times [0, +\infty) \rightarrow \mathbb{R}_+$ is such that $s(x, y, t)$ [$\text{m}^{-2}\text{s}^{-1}$] denotes the source density rate (SDR) of new particles released from cells residing at the surface, and κ_a [ms^{-1}] and κ_d [s^{-1}] are the adsorption and desorption constants, respectively. We will assume here that $c(x, y, z, t) = 0$, $d(x, y, t) = 0$, and $s(x, y, t) = 0$ for $t < 0$, i.e., that before starting the experiment no particles have been generated or are present.

B. Observation model

Our primary interest in (1) lies in characterizing the surface density d at the time T at which it is imaged, in terms of



(a) Particles motion model



(b) Typical observation

Fig. 1. (a) Visualization, at a particle level, of the physical data model described in Section II-A. Three particles, each secreted by a different cell (dark gray) immobilized on the plane (light gray), follow a Brownian motion. When the particles hit the plane, they might bind to it (adsorption; black marks). After a time, they may disassociate (desorption) and continue their Brownian motion. At the end of the experiment, i.e., at time T , they may be free (blue dots) and thus not imaged or bound to the surface (red dot) and thus contribute to the final image. Note that while the relative scale between movement and the pixel size of a potential imaging sensor is consistent with accurate physical parameters, the relative scale of cells and particles was selected for clear visualization. (b) Example section of an image observation from a Fluorospot assay. Here, FITC dye was used as a marker for trapped IFN- γ molecules, and the resulting 512 nm fluorescence was isolated by optic filters and subsequently captured by a color camera at approximately 1 to 1 magnification.

the SDR s . Therefore, we consider the concentration c in the medium to be only an intermediate nuisance parameter. For notational brevity we will write as $\mathbf{r} = (x, y)$ the spatial coordinates of a generic point on the surface $z = 0$, and refer to the final image observation as d_{obs} , i.e., $d_{\text{obs}}(\mathbf{r}) = d(\mathbf{r}, T)$. Note here that while d_{obs} is considered to be exactly equal to the density of particles bound to the surface, in practice, imaging sensors will have different sensitivities and, thus, there will always be a factor of scale $\alpha > 0$, which we will disregard in this paper. Further limitations of imaging sensors, such as finite dimensionality and imperfections in the optical and electrical systems involved, are discussed in Section II-D.

To obtain a suitable characterization of the mapping from s to d_{obs} , we will follow the arguments given in [3] and interchangeably rely on macroscopic arguments pertaining to the evolution of particle distributions, governed by (1), and microscopic arguments pertaining to the behavior of individual particles [44]. Note now that: 1) (1) is a linear system of equations and 2) the homogeneity of (1a) implies that the movement of free particles is independent in the three spatial dimensions. It follows then that the location of a particle originally released at the origin $\mathbf{r} = \mathbf{0}$, will, after a time τ [s]

in Brownian motion with no intermediate binding events, have a distribution over the xy -plane given by the Green function for the homogeneous diffusion equation in 2D during a time τ , i.e., g_σ as in Definition 1 with $\sigma = \sqrt{2D\tau}$ [m] (see [44]).

Definition 1 (Gaussian kernels). $\{g_\sigma : \mathbb{R}^2 \rightarrow \mathbb{R}_+\}_{\sigma>0}$ is a scale family of 2D rotationally invariant Gaussian kernels, where

$$g_\sigma(\mathbf{r}) = \frac{1}{2\pi\sigma^2} \exp\left(-\frac{\mathbf{r}^T\mathbf{r}}{2\sigma^2}\right), \forall \mathbf{r} \in \mathbb{R}^2.$$

Because Brownian motions are Markov processes, it follows that the total displacement over directions in the xy -plane is fully determined by the total time in free motion τ , even when intermediate binding events are present. The total time in free motion of any given particle over some specific time interval is, however, random. Specifically, it depends on the particle's random trajectory, on the collisions of the trajectory with the plane $z = 0$, and on the subsequent random associations (adsorption) and disassociations (desorption), as modeled by (1b) and (1c). Let

$$\varphi : \{(\tau, t) \in [0, T]^2 \mid \tau \leq t\} \rightarrow \mathbb{R}_+, \quad (2)$$

such that $\varphi(\tau, t)$ is the probability (density)¹ of a particle being in free motion for a total time τ before being found in a bound state at time t [s]. $\varphi(\tau, t)$ is defined for $\tau \in [0, t]$ and is determined implicitly by (1). The specific nature of $\varphi(\tau, t)$ is of little relevance to the objective of this section, and only its existence is required. Nonetheless, its characterization will be fundamental for some of the uses of our observation model. In Section II-C, we present a novel and detailed derivation of φ in terms of κ_a , κ_d and D , extending results from [3] by characterizing desorption from the surface in terms of its effect on the total time in free motion.

For a given φ , then, the spatial probability density of finding a particle bound to the surface at time t , after a release into the medium at the origin at time 0, is given by (see [3])

$$p(\mathbf{r}, t) = \int_0^t g_{\sqrt{2D\tau}}(\mathbf{r})\varphi(\tau, t)d\tau,$$

which can be viewed as the Green function for $d(\mathbf{r}, t)$ in (1). Note that $p(\mathbf{r}, t)$ integrated over $\mathbf{r} \in \mathbb{R}^2$ yields the probability that a particle released at time 0 is bound at time t . By linearity, time-invariance, and spatial invariance on the directions in the xy -plane, it follows that d can be expressed as

$$d(\mathbf{r}, t) = (s * p)(\mathbf{r}, t), \quad (3)$$

i.e., as a spatio-temporal convolution of the Green function p and the SDR s . For the spatial part of the convolution in (3), it is convenient to introduce the Gaussian blur operators as follows.

Definition 2 (Gaussian blur operators).

$$\{G_\sigma \in \mathcal{L}(\mathbb{L}^2(\mathbb{R}^2), \mathbb{L}^2(\mathbb{R}^2))\}_{\sigma>0}$$

¹The terms *probability* or *probability density* are technically incorrect in this case. A formal definition of the quantity $\varphi(\tau, t)$ is given in Section II-C.

is a family of convolutional operators, where

$$(G_\sigma f)(\mathbf{r}) = \int_{\mathbb{R}^2} f(\mathbf{r} - \boldsymbol{\rho})g_\sigma(\boldsymbol{\rho})d\boldsymbol{\rho}, \forall f \in \mathbb{L}^2(\mathbb{R}^2),$$

and g_σ is given by Definition 1.

By using Definition 2 and evaluating the convolution in (3) independently over the spatial and temporal dimensions, we can express d compactly as

$$d(\mathbf{r}, t) = \int_0^t G_{\sqrt{2D\tau}} v(\mathbf{r}, \tau, t)d\tau, \quad (4)$$

where $v : \mathbb{R}^2 \times \mathbb{R}_+^2 \rightarrow \mathbb{R}_+$ is such that

$$v(\mathbf{r}, \tau, t) = \int_\tau^t s(\mathbf{r}, t - \eta)\varphi(\tau, \eta)d\eta. \quad (5)$$

v summarizes the effect of movement in the z -dimension, adsorption, and desorption on the diffusion of the particles generated with a source density rate s . Theorem 1 summarizes the conclusions from the discussion above in terms of the image observation d_{obs} . A step-by-step derivation of (4), (5), (6), and (7) from (3) can be found in the supplementary material to this paper.

Theorem 1 (Observation model). Let $d_{\text{obs}} : \mathbb{R}^2 \rightarrow \mathbb{R}_+$ be the spatial density of bound particles at time T , i.e., when the experiment finishes. Then, we have that

$$d_{\text{obs}}(\mathbf{r}) = \int_0^{\sigma_{\text{max}}} G_\sigma a(\mathbf{r}, \sigma)d\sigma, \quad (6)$$

where $\sigma = \sqrt{2D\tau}$, $\sigma_{\text{max}} = \sqrt{2DT}$, and

$$a(\mathbf{r}, \sigma) = \frac{\sigma}{D} v\left(\mathbf{r}, \frac{\sigma^2}{2D}, T\right), \quad (7)$$

with v as in (5). We will refer to $a : \Omega \rightarrow \mathbb{R}_+$ in (7) as the post adsorption-desorption source density rate (PSDR).

An important feature of (6) is that the spatial properties of s are retained by a , as (5) and (7) operate only on the temporal dimension. This implies that the PSDR a contains the same amount of information for SL as the original SDR s .

The value of the PSDR $a(\mathbf{r}, \sigma)$ can be interpreted as the density of particles released from a location \mathbf{r} that will appear in d_{obs} after a 2D diffusion of $\tau = \sigma^2/(2D)$. The model in (4), however, is not a 2D diffusion model with an equivalent source v , due to the dependence of v on the observation time t . Nonetheless, we can and will treat (6) as our observation model with a , rather than s , as the sought unknown quantity. This will result in a few important benefits. First, the relative simplicity of (6) will prove beneficial both for formulating the inverse diffusion problem and for constructing its algorithmic solution. Second, the recovery of a in (7) can be addressed without an explicit characterization of φ . This removes the need for the values of κ_a , κ_d and D , which can vary between assays, are costly to measure [29], and hard to estimate [38]. This said, an explicit characterization of φ is still desirable. In particular, it could enable the recovery of the original SDR s from the recovered a , and it allows for simulation of data based on a given SDR s , which is easier to postulate than the PSDR a . We therefore continue by providing an explicit

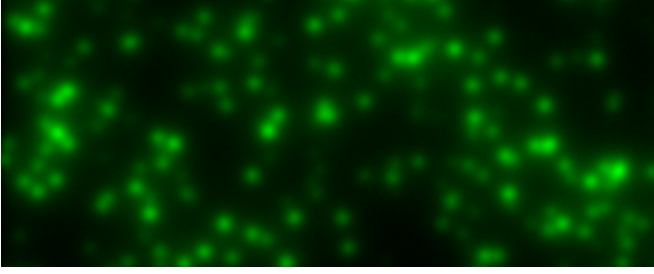


Fig. 2. Example section of an image simulated from model (1) using the result in Theorem 2, observed through a simulated imperfect, noisy image acquisition system. The image is loaded into the green channel for ease of comparison with Fig. 1. For details on the discretization and numerical techniques employed to obtain this image, see Section IV, Section II-C, and the supplementary material to this paper.

characterization of φ that exhibits favorable properties with regards to its numerical approximation.

C. Physical parameters and data synthesis

The quantity $\varphi(\tau, t)$ summarizes the relation between the time t at which a particle released at time 0 is found bound, and the total time τ it has spent in free movement. Formally, consider a particle released at time 0 and let its position in the z -dimension be $\{z_t\}_{t \in [0, T]}$. For each $t \in [0, T]$, consider the random variables $\tau = |\{\tilde{\tau} \in [0, t] : z_{\tilde{\tau}} > 0\}|$, i.e., the time in free motion before t , and $b_t \in \{0, 1\}$ such that $b_t = 1$ if $z_t = 0$ and $b_t = 0$ otherwise, i.e., an indicator of the particle being bound² at time t . Then, $\varphi(\tau, t)$ is formally the Radon-Nikodym derivative of the joint distribution of the continuous random variable τ and the discrete random variable b_t , i.e., $\forall \tau \in [0, t]$,

$$\varphi(\tau, t) = f_{\tau|b_t}(\tau|b_t = 1) \Pr(b_t = 1),$$

where $f_{\tau|b_t}(\cdot|b_t = 1)$ is the probability density function of the time in free motion τ given that the particle is found bound at time t .

Obtaining a characterization of $\varphi(\tau, t)$ in terms of κ_a , κ_d and D provides further possibilities to exploit the model (6). First, one can use this model to obtain synthetic data that corresponds to specific reaction-diffusion-adsorption-desorption models and specific source density rates $s(\mathbf{r}, t)$, which provides a way of objectively comparing algorithmic proposals. Second, one could, if the physical parameters of a real assay were known, address the inverse problem of obtaining $s(\mathbf{r}, t)$ from any estimation of $a(\mathbf{r}, \sigma)$ by inverting the linear system formed by equations (5) and (7). In Theorem 2, we provide the full characterization of $\varphi(\tau, t)$ in terms of the physical parameters of the model. Both Theorem 2 and Lemma 1, an intermediate result, are proved in Appendix A. In Fig. 2, we show a section of a synthetic image generated using the result in Theorem 2, for comparison with the image obtained from a real Fluorospot assay in Fig. 1.

Consider first a characterization of the simpler case $\kappa_d = 0$, i.e., the case in which particles that are bound to the surface can not be desorbed, which we present in Lemma 1.

²Note here that the event $z_t = 0$ is equivalent to the particle being bound ($b_t = 1$) because under a free Brownian motion, $z_t = 0$ has probability 0.

Lemma 1 (Characterization of the observation model from physical parameters, Case $\kappa_d = 0$). *Consider model (1) when $\kappa_d = 0$. Then, we have that $\varphi(\tau, t) = i_{[0, t]}(\tau)\phi(\tau)$, with*

$$\phi(\tau) = \frac{\kappa_a}{\sqrt{\pi D \tau}} - \frac{\kappa_a^2}{D} \operatorname{erfcx} \left(\kappa_a \sqrt{\frac{\tau}{D}} \right), \quad (8)$$

where

$$\operatorname{erfcx}(x) = e^{x^2} \operatorname{erfc}(x), \text{ and } \operatorname{erfc}(x) = \frac{2}{\sqrt{\pi}} \int_x^\infty e^{-t^2} dt,$$

are the scaled-complementary and complementary error functions, respectively.

Theorem 2 extends this result to the general case in which $\kappa_d \geq 0$ by segmenting the total time of free motion in subsequent fractions of free motion interrupted by adsorption-desorption events.

Theorem 2 (Characterization of the observation model from physical parameters). *Consider model (1). Then, we have that*

$$\varphi(\tau, t) = i_{[0, t]}(\tau) \sum_{j=1}^{\infty} \phi^{j*}(\tau) p[j-1; \kappa_d(t-\tau)], \quad (9)$$

where $\phi^{j*}(\tau)$ is the j -th convolutional power of $\phi(\tau)$ in (8) and

$$p[j; \lambda] = \frac{\lambda^j e^{-\lambda}}{j!}, \forall j \in \mathbb{N}, \forall \lambda \geq 0, \quad (10)$$

is the probability mass function of a Poisson random variable with mean λ evaluated at j .

Note that [43] also studied model (1) with $\kappa_d \geq 0$, but in terms of an expression for the distribution of particles in the z -dimension after a time t since they were released, i.e. a parallel to the $u(z, t)$ used in Appendix A to prove Lemma 1. However, because our goal is to characterize the total time in free motion, and $u(z, t)$ does not reveal how a particle arrived at a position z at time t , our result in Theorem 2 is needed.

For any practical application, $\varphi(\tau, t)$ needs to be computed, i.e. approximated and discretized in some manner. To this end, note that truncating (9) at a finite J_ϵ can be done at any arbitrary error level $\epsilon > 0$. Intuitively, this is because $p[j; \lambda]$ decays exponentially for large j s while $\phi^{j*}(\tau)$ is stable (in norm) with j . Formally, this result is stated in Lemma 2 and proved in Appendix A.

Lemma 2 (Truncation of the sum to characterize the model). *Consider, for any $\epsilon > 0$,*

$$J_\epsilon = Q_{\text{Poi}} \left(1 - \frac{\epsilon}{\|\phi\|_{L^2(0, +\infty)}^2}; \kappa_d T \right),$$

where $Q_{\text{Poi}}(p; \lambda)$ is the quantile function, i.e. the inverse cumulative distribution function, of a Poisson random variable with mean $\lambda > 0$ evaluated at $p \in (0, 1)$. Then,

$$\tilde{\varphi}(\tau, t) = \left| \varphi(\tau, t) - \sum_{j=1}^{J_\epsilon-1} \phi^{j*}(\tau) p[j-1; \kappa_d(t-\tau)] \right| \leq \epsilon,$$

$\forall (\tau, t) \in [0, T]^2$ such that $\tau \leq t$.

Finally, note that a discrete approximation to the j -th convolutional power $\phi^{j*}(\tau)$ can be computed numerically by discretization of $\phi(\tau)$ and recursive discrete convolution.

D. Model flexibility and Imaging limitations

To assume that an imaging system can provide measurements given by (6) is, naturally, an idealization. Besides finite dimensionality, which will be treated in detail in Section IV, any physically feasible image acquisition must deviate from this model due to the following factors: 1) random photonic and electronic events, often modeled by additive white noise in the final observation, 2) non-linear effects, such as limited dynamic ranges or quantization, 3) linear effects, such as a blur with a point-spread function (PSF) that limits the resolution of a particular optical system, and 4) a bounded field of view.

In terms of the effect of random events, we will numerically demonstrate in Part II of this paper [13, Section III] that our approach to SL is very robust to the presence of additive white noise. In terms of non-linear effects, we assume that the dynamic range of the camera is adjusted automatically so that saturation is not an issue. Additionally, we implicitly assume that the imaging sensor is noise-limited instead of quantization-limited, as is the case with most current cameras. In our empirical validation on synthetic data in Part II [13, Section III], we enforce this by using a statistical model for quantization to ensure that the levels of additive noise under analysis are much larger than those expected from quantization error in a current scientific camera, e.g., 12-bit quantization. In terms of linear effects, we will assume that the PSF for the optical system is monomodal and symmetric, and well approximated by a Gaussian kernel g_{σ_b} with some standard deviation σ_b . Under these assumptions, we modify (6) to express the blurred observation d_{obs}^b as

$$d_{\text{obs}}^b = g_{\sigma_b} * d_{\text{obs}} = \int_0^{\sigma_{\max}} G_{\sigma+\sigma_b} a_{\sigma} d\sigma. \quad (11)$$

All of the results in this two-part paper are invariant to this shift in σ and can be re-derived mutatis mutandis for (11). Finally, in terms of the limited field of view, we will make the reasonable assumption that all the sources we aim at recovering are within the camera's field of view.

III. INVERSE DIFFUSION BY FUNCTIONAL OPTIMIZATION

A. Optimization problems for inverse diffusion

In this section, we first present the inverse problem of recovering the PSDR a from the density of bound analyte d_{obs} as a non-negative minimum-norm functional optimization problem. Then, we propose to address the ill-posedness of this naïve minimum-norm formulation by regularizing it according to the available prior knowledge. As a result, we propose a non-negative group-sparsity regularized minimum-norm optimization problem to fit the observation model in Section II to the data.

Our treatment and language will be that of functional analysis, which will enable the exposition of the optimization problem in the natural spaces of particle densities. Although discretization will eventually be necessary for the synthesis

and analysis of data, introducing it already in the observation model (6) would mask the generality of the proposed approach. Indeed, in Section IV we propose a simple discretization scheme for (6) and any functional algorithm for inverse diffusion, but our exposition opens up inverse diffusion to the use of more sophisticated discretization schemes. For example, off-the-grid solutions such as [45] dynamically estimate the support of a discrete measure observed through a convolutional operator, and offer opportunities for more rigorous mathematical analysis. In conclusion, in a philosophy strongly supported by [46, ch. 5], we present an optimization problem to address inverse diffusion on a functional (infinite-dimensional) setting and discretize the problem only after that. Similarly, in Part II [13], we propose first the functional version of the algorithm, and use the simple discretization in Section IV only after that to provide an implementable algorithm and empirical results.

We begin by introducing the Hilbert spaces needed to properly state the inverse problem. The definitions of these function spaces will permit the adaptation of the problem to specific, practical conditions. For instance, in defining the space of observed densities, we include a weighting function that enables us to, in each case, set a value on the cost of wrongly predicting the observed density in each location. This allows us, for example, to make the inverse problem robust to regions of an image sensor that are known beforehand to be faulty or irrelevant.

Definition 3 (Observed density space). *Consider a weighting function $w \in L_+^{\infty}(\mathbb{R}^2)$ such that $w \neq 0$. Then, the bilinear form*

$$(d_1|d_2)_{\mathcal{D}} = \int_{\mathbb{R}^2} w^2(\mathbf{r})d_1(\mathbf{r})d_2(\mathbf{r})d\mathbf{r}, \quad \forall d_1, d_2 : \mathbb{R}^2 \rightarrow \mathbb{R},$$

is positive and symmetric. Therefore, the linear space

$$\mathcal{D} = \{d : \mathbb{R}^2 \rightarrow \mathbb{R} : (d|d)_{\mathcal{D}} < +\infty\},$$

equipped with the inner product $(\cdot|\cdot)_{\mathcal{D}}$ is a Hilbert space, and it is where the observed density lies, i.e., $d_{\text{obs}} \in \mathcal{D}_+$.

Similarly, in defining the space of PSDRs, we include a masking pattern that indicates which locations can hold cells and which cannot. This reduces the support of the considered PSDRs, thus making the inverse problem easier by incorporating prior knowledge.

Definition 4 (PSDR space). *Consider a masking pattern function $\mu : \mathbb{R}^2 \rightarrow \{0, 1\}$ with a non-empty bounded support $\text{supp}(\mu)$. Then, the linear space*

$$\mathcal{A} = \{a \in L^2(\Omega) : \text{supp}(a) \subseteq \text{supp}(\mu) \times [0, \sigma_{\max}]\},$$

equipped with the inner product $(\cdot|\cdot)_{\mathcal{A}} = (\cdot|\cdot)_{L^2(\Omega)}$ is a Hilbert space, and it is the space where the PSDR lies, i.e., $a \in \mathcal{A}_+$. Here, recall that $\Omega = \mathbb{R}^2 \times \mathbb{R}_+$.

The core of the observation model in Theorem 1 is the operator that reflects how a change in the PSDR $a \in \mathcal{A}_+$ affects the observed density $d_{\text{obs}} \in \mathcal{D}_+$, i.e., the observation operator in this inverse problem. We refer to it as the diffusion operator because of the parallelism between d_{obs} and an

observation of a 2D diffusion process with SDR v , which we discussed at the end of Section II-B.

Definition 5 (Diffusion operator). *The linear operator $A : \mathcal{A} \rightarrow \mathcal{D}$ such that*

$$Aa = \int_0^{\sigma_{\max}} G_{\sigma} a_{\sigma} d\sigma, \forall a \in \mathcal{A},$$

represents the dependence between a and d_{obs} specified by Theorem 1. Here, $a_{\sigma} : \mathbb{R}^2 \rightarrow \mathbb{R}_+$ is such that $a_{\sigma}(\mathbf{r}) = a(\mathbf{r}, \sigma)$, $\forall (\mathbf{r}, \sigma) \in \Omega$.

The measurement model (6) can now be succinctly expressed as $d_{\text{obs}} = Aa$. In this view, the estimation of the PSDR a may be addressed as a least squares problem with respect to the operator A , i.e., as the convex optimization problem

$$\min_{a \in \mathcal{A}} \left[\|Aa - d_{\text{obs}}\|_{\mathcal{D}}^2 + \delta_{\mathcal{A}_+}(a) \right]. \quad (12)$$

Here, the penalty function for the prediction Aa is precisely the square of the norm $\|\cdot\|_{\mathcal{D}}$ on the space of observations, which takes into account the weighting w to determine the importance of an error in each of the different spatial positions. Additionally, for the PSDR to have physical meaning, the positivity constraint $a \in \mathcal{A}_+$ has to be met. Note that $\mathcal{A}_+ \subset \mathcal{A}$ is a convex cone, and that the indicator function notation for the convex constraint is convenient for later treatment.

Because the dimensionality of the PSDR a exceeds that of the observation d_{obs} , (12) is ill-posed in the sense that many different PSDRs lead to the same observation. This calls for the use of a regularizer that eases the inverse problem by biasing the solution towards more plausible explanations. In particular, we propose to use a non-negative group-sparsity regularizer to induce group behavior in the σ -dimension and sparsity in the spatial dimensions. This is consistent with the explanation of the bound density d_{obs} as a result of particle generation by a finite number of spatially separated, immobilized cells. Therefore, we propose to solve the optimization problem

$$\min_{a \in \mathcal{A}} \left[\|Aa - d_{\text{obs}}\|_{\mathcal{D}}^2 + \delta_{\mathcal{A}_+}(a) + \lambda \left\| \left\| \xi a_{\mathbf{r}} \right\|_{L^2(\mathbb{R}_+)} \right\|_{L^1(\mathbb{R}^2)} \right] \quad (13)$$

which is convex and suited to iterative non-smooth convex optimization methods, as we show in Part II [13]. Here, for each $\mathbf{r} \in \mathbb{R}^2$, $a_{\mathbf{r}} : [0, \sigma_{\max}] \rightarrow \mathbb{R}_+$ is such that $a_{\mathbf{r}}(\sigma) = a(\mathbf{r}, \sigma)$ for any $\sigma \in [0, \sigma_{\max}]$, $\lambda > 0$ is the regularization parameter, and $\xi \in L_+^{\infty}[0, \sigma_{\max}]$ is a non-negative bounded weighting function in σ that can be used to incorporate further prior knowledge. For example, if one knew the exact parameters κ_a , κ_d and D of the physical system, one could use the characterization of φ in Theorem 2 to choose ξ so that the penalization in (13) corresponds to a uniform penalization through t in the original SDR s . Additionally, if one knew that the particular experimental setting only allows for cells to generate particles during times t such that $t_0 < t < t_1 < T$, one could choose ξ to have very large values for $\sigma \in [0, \sqrt{2Dt_1}] \cup [\sqrt{2D(T-t_0)}, \sigma_{\max}]$. Finally, if one wanted to impose the restrictions of the model only on a certain range of σ s, say $\sigma \in \mathfrak{N} \subset [0, \sigma_{\max}]$, and relax them for its complement $\mathfrak{N}^c = [0, \sigma_{\max}] \setminus \mathfrak{N}$, one could choose ξ

such that $\text{supp}(\xi) = \mathfrak{N}$. The case in which ξ is simply the $(0, 1)$ -indicator function of a set \mathfrak{N} is of special relevance in Part II [13] due to its tractability, and is useful, for example, to use the values of a for $\sigma \in \mathfrak{N}^c$ to account for a low-frequency background that could not be explained by cell secretion alone.

Note now that while in both (12) and (13) we have used \min instead of \inf , we have yet been unable to formally prove that these problems do have a minimizer in \mathcal{A}_+ . Nonetheless, in the following section we provide some results that characterize the diffusion operator A , providing some insight on its structure and beneficial properties. Some of these results will enable us to prove, in Section IV, that the discretized equivalents to (12) and (13) under our discretization scheme do have a minimizer.

B. Characterization of the diffusion operator

First, we verify that A is a continuous, i.e., bounded, linear operator. Although this does not provide the existence of a minimizer of (12) or (13), it does give some intuitive hope in terms of the bounded inverse theorem.

Lemma 3 (Boundedness of the diffusion operator). *The norm in $\mathcal{L}(\mathcal{A}, \mathcal{D})$ of the linear operator $A : \mathcal{A} \rightarrow \mathcal{D}$ in Definition 5 is bounded as*

$$\|A\|_{\mathcal{L}(\mathcal{A}, \mathcal{D})} \leq \sqrt{\sigma_{\max}} \|w\|_{L^{\infty}(\mathbb{R}^2)}.$$

Thus, A is a bounded operator and, because A is linear, A is a linear continuous operator, i.e. $A \in \mathcal{L}(\mathcal{A}, \mathcal{D})$.

We proceed by characterizing the nullspace of the operator, showing that it only contains a very specific class of functions. This rather simple result, which is also valid for any convolutional operator with non-negative unit L^1 -norm kernel, will be of great help when characterizing the existence of minimizers in the discrete case.

Lemma 4 (Nullspace of the diffusion operator). *Consider the nullspace of the diffusion operator, i.e., $\mathcal{N}(A) = \{a \in \mathcal{A} : Aa = 0\}$. Then, $\forall a \in \mathcal{N}(A)$, we have that $\|a_+\|_{L^1(\Omega)} = \|a_-\|_{L^1(\Omega)}$.*

Note that an immediate consequence of Lemma 4 is that $\mathcal{A}_+ \cap \mathcal{N}(A) = \{0\}$, since $a \in \mathcal{A}_+$ implies $\|a_-\|_{L^1(\Omega)} = 0$, which, if $a \in \mathcal{N}(A)$, implies that $\|a_+\|_{L^1(\Omega)} = 0$, i.e., $a = a_+ + a_- = 0$.

For the sake of completeness, we also present here the expression for the adjoint operator A^* of the diffusion operator A , which will be of great value in the design of algorithms to minimize (13) in Part II [13].

Lemma 5 (Adjoint to the diffusion operator). *The adjoint operator $A^* \in \mathcal{L}(\mathcal{D}, \mathcal{A})$ to the diffusion operator A in Definition 5 is such that*

$$(A^*d)(\mathbf{r}, \sigma) = \mu(\mathbf{r}) \cdot (G_{\sigma} \{w^2 d\})(\mathbf{r}), \forall d \in \mathcal{D},$$

for each $\mathbf{r} \in \mathbb{R}^2$ and $\sigma > 0$.

Both Lemma 3 and Lemma 5 are based on an equivalent characterization of the family of Gaussian blur operators $\{G_{\sigma}\}$ from Definition 2, based on standard results for convolutional operators. This characterization, i.e., Properties 1 and 2, can

be found together with the proof for the results in this section in Appendix B.

IV. DISCRETIZATION

In practice, no imaging sensor is infinitely resolute. A digital camera will instead obtain a matrix $\tilde{d}_{\text{obs}} \in \mathbb{T}_+(M, N)$, which will be some discretization of d_{obs} in (6). Here, $M, N \in \mathbb{N}$ represent the number of pixels in each dimension of the imaging sensor, with typical values of 1024 or 2048 for current scientific cameras. In particular, the relation between \tilde{d}_{obs} and d_{obs} in a generic discrete imaging sensor can be modeled by the operator $R_{\mathcal{D}} : \mathcal{D} \rightarrow \mathbb{T}(M, N)$ such that

$$\tilde{d} = R_{\mathcal{D}}(d) = \left(\tilde{d}_{m,n} \right) = \left[\int_{\Lambda_{m,n}} d(\mathbf{r}) \, d\mathbf{r} \right], \quad (14)$$

$\forall d \in \mathcal{D}$, where $m \in \{1, 2, \dots, M\}$, $n \in \{1, 2, \dots, N\}$ and $\Lambda_{m,n} = \{(m, n)\} + [-0.5, 0.5]^2$ is the region that corresponds to the pixel at the position (m, n) . Here, the scale of each spatial variable is normalized with respect to the pixel size to simplify further derivations. Additionally, each spatial variable is translated so that $(1, 1)$ corresponds to the location of the first pixel's center. Note that in order to preserve consistency, normalization is also needed on the σ -dimension in (6)–(7), i.e., we will work with $\tilde{\sigma} = \sigma / \Delta_{\text{pix}}$ and $\tilde{\sigma}_{\text{max}} = \sigma_{\text{max}} / \Delta_{\text{pix}}$, where Δ_{pix} [m] is the length of a pixel's side.

In the classical theory of discretization [47, Ch. 34–35], one wants to numerically solve a functional inverse problem, e.g., find $a \in \mathcal{A}_+$ such that $Aa = d_{\text{obs}}$ for a specific $d_{\text{obs}} \in \mathcal{D}_+$. Then, to do so numerically, one defines a discretization scheme parametrized by the dimensionalities $q_1, q_2 \in \mathbb{N}$ of the observation and solution, i.e., some rule to obtain approximations

$$\tilde{A}_{q_1, q_2} \in \mathbb{T}(q_1, q_2), \tilde{a}_{q_1} \in \mathbb{R}^{q_1}, \tilde{d}_{\text{obs}, q_2} \in \mathbb{R}^{q_2},$$

and one solves $\tilde{A}_{q_1, q_2} \tilde{a}_{q_1} = \tilde{d}_{\text{obs}, q_2}$ instead, relying on equivalence results when $q_1, q_2 \rightarrow +\infty$. In our case, we want to solve the functional optimization problem proposed in (5), but only have access to a discretized observation $\tilde{d}_{\text{obs}} = R_{\mathcal{D}}(d_{\text{obs}})$. This imposes the structure in (14) onto our discretization of the image observation d_{obs} , and fixes its dimension to $q_2 = M \times N$. With respect to (13), we will assume that the user-specified parameters μ , w and ξ are chosen consistently with the discretization. For example, we will assume that instead of a weighting function $w(\mathbf{r})$, we have a weighting matrix $\tilde{w} = R_{\mathcal{D}}(w) \in \mathbb{T}(M, N)$, at the same discretization level as \tilde{d}_{obs} .

Classical results in discretization theory [47] cover only cases in which the functional inverse problem is well-posed. In fact, the design of discretization schemes in the context of possibly ill-posed inverse problems, such as (13), is an open research topic [48]–[51]. Thus, formulating a discretization that is optimal in some sense is beyond the scope of this paper. Instead, we will use the basic ideas from inner approximation schemes [47, Ch. 34] to propose an intuitively natural discretization.

A discretization scheme for (13) under the inner approximation paradigm involves two restriction operators, i.e.

$$R_{\mathcal{A}} : \mathcal{A} \rightarrow \mathcal{A}_{q_1}, R_{\mathcal{D}} : \mathcal{D} \rightarrow \mathcal{D}_{q_2},$$

where \mathcal{A}_{q_1} and \mathcal{D}_{q_2} are q_1 - and q_2 -dimensional spaces, respectively, and $R_{\mathcal{D}}$ is characterized in (14) with $\mathcal{D}_{q_2} = \mathbb{T}(M, N)$ and two extension operators, i.e.

$$E_{\mathcal{A}} : \mathcal{A}_{q_1} \rightarrow \mathcal{A}, E_{\mathcal{D}} : \mathcal{D}_{q_2} \rightarrow \mathcal{D}.$$

These operators fully characterize the discretization scheme, because they not only determine the discrete approximation of each element in \mathcal{A} or \mathcal{D} through the restriction operators, but also the discrete approximation of any operator from and to these spaces. In our case, we are specifically interested in the finite-dimensional approximation of the diffusion operator A under a given discretization scheme, which can be used directly to synthesize data, but also will be a fundamental step in any discrete iterative procedure to approximate a solution to (13). The latter also applies to finding the discrete expression for the adjoint A^* , which will play an important role in any discrete algorithm that aims to exploit the smoothness of the square norm $\|Aa - d_{\text{obs}}\|_{\mathcal{D}}^2$ in (13). Given a discretization scheme, these finite-dimensional approximations are the operators $\tilde{A} : \mathcal{A}_{q_1} \rightarrow \mathcal{D}_{q_2}$ and $\tilde{A}^* : \mathcal{D}_{q_2} \rightarrow \mathcal{A}_{q_1}$ such that [47, p. 964]

$$\tilde{A}\tilde{a} = R_{\mathcal{D}}(A E_{\mathcal{A}}[\tilde{a}]), \forall \tilde{a} \in \mathcal{A}_{q_1}, \quad (15a)$$

$$\tilde{A}^*\tilde{d} = R_{\mathcal{A}}(A^* E_{\mathcal{D}}[\tilde{d}]), \forall \tilde{d} \in \mathcal{D}_{q_2}. \quad (15b)$$

Similarly, any operators $B_1 : \mathcal{A} \rightarrow \mathcal{A}$, $B_2 : \mathcal{D} \rightarrow \mathcal{D}$ will be approximated within the discretization scheme by $\tilde{B}_1 : \mathcal{A}_{q_1} \rightarrow \mathcal{A}_{q_1}$ and $\tilde{B}_2 : \mathcal{D}_{q_2} \rightarrow \mathcal{D}_{q_2}$ such that

$$\tilde{B}_1\tilde{a} = R_{\mathcal{A}}(B_1 E_{\mathcal{A}}[\tilde{a}]), \forall \tilde{a} \in \mathcal{A}_{q_1}, \quad (16a)$$

$$\tilde{B}_2\tilde{d} = R_{\mathcal{D}}(B_2 E_{\mathcal{D}}[\tilde{d}]), \forall \tilde{d} \in \mathcal{D}_{q_2}, \quad (16b)$$

and any functional $\vartheta : \mathcal{A} \rightarrow \mathbb{R}$ will be approximated by $\tilde{\vartheta} : \mathcal{A}_{q_1} \rightarrow \mathbb{R}$ such that

$$\tilde{\vartheta}(\tilde{a}) = \vartheta(E_{\mathcal{A}}[\tilde{a}]), \forall \tilde{a} \in \mathcal{A}_{q_1}. \quad (17)$$

In our particular case, we have chosen the following restriction and extension operators, and through them, a specific discretization. The restriction operator for \mathcal{D} is given by the camera and fulfills (14). For restricting \mathcal{A} , then, we propose using

$$R_{\mathcal{A}}(a) = \left(\tilde{a}_{m,n,k} \right) = \left[\frac{1}{\sqrt{\Delta_k}} \int_{\Lambda_{m,n,k}} a(\mathbf{r}, \sigma) \, d\mathbf{r} d\sigma \right], \quad (18)$$

with $\mathcal{A}_{q_1} = \mathbb{T}(M, N, K)$, m, n as above, $k \in \{1, 2, \dots, K\}$, $\Lambda_{m,n,k} = \Lambda_{m,n} \times [\tilde{\sigma}_{k-1}, \tilde{\sigma}_k]$ and $\Delta_k = (\tilde{\sigma}_k - \tilde{\sigma}_{k-1})$, with $\{\tilde{\sigma}_0, \tilde{\sigma}_1, \dots, \tilde{\sigma}_K\}$ an arbitrary grid in the $\tilde{\sigma}$ -dimension such that $\tilde{\sigma}_{k-1} < \tilde{\sigma}_k$, $\tilde{\sigma}_0 = 0$ and $\tilde{\sigma}_K = \tilde{\sigma}_{\text{max}}$. As mentioned before, this discretization is also assumed in user parameters that concern $a(\mathbf{r}, \sigma)$, i.e., $\tilde{\mu} \in \mathbb{T}(M, N)$ is considered as a mask in the finite-dimensional spatial coordinates and $\tilde{\xi} \in \mathbb{R}_+^K$ is considered as a non-negative weighting vector across ks . For the latter, note that if ξ has the structure discussed at the end of Section III-A, i.e., it is the $(0, 1)$ -indicator of a set $\mathfrak{N} \subset [0, \sigma_{\text{max}}]$, this set will be aligned with respect to the discretization boundaries $\tilde{\sigma}_k$, and an equivalent set of discrete indexes $\mathfrak{N} = \{k \in \{1, 2, \dots, K\} : (\tilde{\sigma}_{k-1}, \tilde{\sigma}_k) \subset \mathfrak{N}\}$ can be defined.

For the extension operators, we use the inner approximation interpretation of the discrete spaces $\mathcal{A}_{q_1} \subset \mathcal{A}$ and $\mathcal{D}_{q_2} \subset \mathcal{D}$, and consider them as parameterizations of piece-wise constant functions in \mathcal{A} and \mathcal{D} , i.e.

$$E_{\mathcal{D}}(\tilde{d}) = \sum_{n=1}^N \sum_{m=1}^M \tilde{d}_{m,n} i_{\Lambda_{m,n}}, \quad (19)$$

and

$$E_{\mathcal{A}}(\tilde{a}) = \sum_{n=1}^N \sum_{m=1}^M \sum_{k=1}^K \frac{1}{\sqrt{\Delta_k}} \tilde{a}_{m,n,k} i_{\Lambda_{m,n,k}}, \quad (20)$$

with $i_{\Lambda_{m,n}}$ and $i_{\Lambda_{m,n,k}}$ the $(0, 1)$ -indicator functions for $\Lambda_{m,n}$ and $\Lambda_{m,n,k}$, respectively.

An example of the structure chosen for the discretization of \mathcal{A} is portrayed in Fig. 3. Because the camera's restriction operator (14) fixed the understanding of the spatial domain in \mathcal{D} as a regular grid, it was natural to use the same regular grid structure for the spatial dimension in the discretization of \mathcal{A} too. The discretization of the σ -dimension, however, could have been addressed much differently, for example, using a more flexible function basis in (20). However, we opted to use an irregular grid in σ , which provides modeling flexibility and preserves mathematical tractability.

In terms of the dimensionality of the problem, our choices imply that \mathcal{A} is discretized with the same spatial resolution as the observation \tilde{d}_{obs} . A finer resolution in this discretization would yield super-resolution in the recovery of the PSDR and, therefore, more accurate SL. However, even with the modest typical values $M = N = 512$ and $K = 8$ used in our numerical evaluations in Part II [13], our choice already results in a discretized inverse problem with $q_1 \approx 2 \cdot 10^6$ optimization variables. In real scenarios, like the one introduced in Section V-A, these values are $M = N = 2048$ and $K = 6$, which result in $q_1 \approx 25 \cdot 10^6$ unless the resolution of the sensor is artificially decreased. Therefore, we have left further inquiries into grid-based super-resolution methods outside of the scope of this paper.

Direct computation of (15) using the particular restriction and extension operators (14), (18), (19), and (20) yields

$$\tilde{A}\tilde{a} = \sum_{k=1}^K \tilde{g}_k \circledast \tilde{a}_k, \quad (21)$$

$$\tilde{A}^* \tilde{d} = \left(\tilde{\mu} \circledast \left(\tilde{g}_k \circledast \left[\tilde{w}^2 \circledast \tilde{d} \right] \right) \right), \quad (22)$$

for $k \in \{1, 2, \dots, K\}$, where \cdot^2 refers to element-wise squaring, \circledast to the Hadamard (element-wise) product, \circledast to discrete convolution with zero-padding, $\tilde{a}_k \in \mathbb{T}(M, N)$ for $k \in \{1, 2, \dots, K\}$ to the different cuts in the k -dimension in \tilde{a} , and $g_k : \mathbb{Z}^2 \rightarrow \mathbb{R}_+$ for $k \in \{1, 2, \dots, K\}$ to the discrete convolutional kernels such that

$$\tilde{g}_k(\tilde{\mathbf{r}}) = \frac{1}{\sqrt{\Delta_k}} \int_{\tilde{\sigma}_{k-1}}^{\tilde{\sigma}_k} \int_{\Lambda_{0,0}^2} g_{\tilde{\sigma}}(\tilde{\mathbf{r}} + \boldsymbol{\rho}_1 - \boldsymbol{\rho}_2) d\boldsymbol{\rho}_1 \times d\boldsymbol{\rho}_2 d\tilde{\sigma},$$

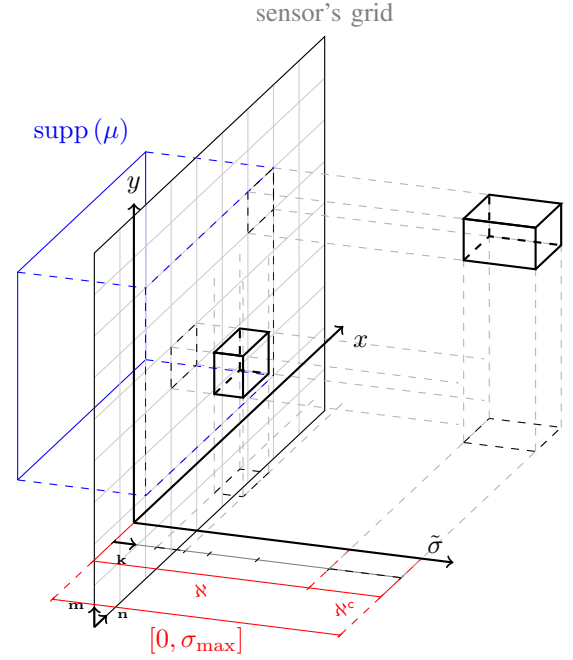


Fig. 3. Example of a discretization grid for \mathcal{A} with $M = N = 9$, $K = 6$. Highlighted, $\Lambda_{5,4,2}$ and $\Lambda_{7,7,6}$. In gray, is the sensor's grid, which coincides with the spatial grid for \mathcal{A} and the resolution of the recovered PSDR. In blue, is the support of a mask $\mu(\mathbf{r})$ that specifies where particle sources can be located. Note that the particular support can also be specified in terms of a mask matrix $\tilde{\mu}$. In red, are the sets \mathbb{N} and \mathbb{N}^c that characterize the behavior of ξ . Note that here, $\mathbb{N} = \{1, 2, \dots, 5\}$ and $\mathbb{N}^c = \{6\}$.

for any $\tilde{\mathbf{r}} \in \mathbb{Z}^2$. Note that, because $g_{\tilde{\sigma}}$ is an isotropic 2D Gaussian probability density function, it is separable in the different spatial dimensions, and, therefore

$$\tilde{g}_k[(m, n)] = \frac{1}{\sqrt{\Delta_k}} \int_{\tilde{\sigma}_{k-1}}^{\tilde{\sigma}_k} \omega_{\tilde{\sigma}}(m) \omega_{\tilde{\sigma}}(n) d\tilde{\sigma}, \quad (23)$$

$\forall (m, n) \in \mathbb{Z}^2$ with $\omega_{\tilde{\sigma}} : \mathbb{Z} \rightarrow \mathbb{R}_+$ such that for any $m \in \mathbb{Z}$, [52]

$$\omega_{\tilde{\sigma}}(m) = \int_{-\frac{1}{2}}^{\frac{1}{2}} \left[\Phi\left(\frac{m + \rho + \frac{1}{2}}{\tilde{\sigma}}\right) - \Phi\left(\frac{m + \rho - \frac{1}{2}}{\tilde{\sigma}}\right) \right] d\rho,$$

where $\Phi : \mathbb{R} \rightarrow [0, 1]$ is the standard 1D normal cumulative density function. The detailed derivation of the expressions (21), (22) and (23), as well as insights on techniques for the numerical computation of (23), can be found in the supplementary material to this paper.

Using the proposed discretization scheme we obtain a discretized equivalent to (13), i.e., the finite-dimensional optimization problem

$$\min_{\tilde{a}} \left\{ \left\| \tilde{A}\tilde{a} - \tilde{d}_{\text{obs}} \right\|_{\tilde{w}}^2 + \lambda \sum_{m,n} \left\| \tilde{\xi} \circledast \tilde{a}_{m,n} \right\|_2 \right\}, \quad (24)$$

subject to $\tilde{a} \in \mathbb{T}_+(M, N, K)$, where $\|\cdot\|_{\tilde{w}}$ denotes the finite-dimensional \tilde{w} -weighted Euclidean norm, and $\tilde{a}_{m,n} \in \mathbb{R}^K$. Now, the finite dimensionality of the problem enables us to rely on the extreme-value theorem for deriving the existence of a minimizer of (24) from the closed and bounded sublevel sets given by the regularizer when $\lambda > 0$ and $\xi_k > 0$ for any

k , or from those of the data penalty term if $\tilde{\xi}_k = 0$ for some k or $\lambda = 0$. This is summarized in Lemma 6.

Lemma 6 (Existence of a solution to the discretized problem). *Consider the function $C : \mathbb{T}(M, N, K) \rightarrow \bar{\mathbb{R}}$ such that $C(\tilde{a}) = \left\| \tilde{d}_{\text{obs}} - \tilde{A}\tilde{a} \right\|_{\tilde{w}}^2 + f(\tilde{a})$, with $f : \mathbb{T}(M, N, K) \rightarrow \bar{\mathbb{R}}$ such that*

$$f(\tilde{a}) = \delta_{\mathbb{T}_+(M, N, K)}(\tilde{a}) + \lambda \sum_{m, n} \left\| \tilde{\xi} \odot \tilde{a}_{m, n} \right\|_2.$$

Then, if either $\lambda > 0$ and $\tilde{\xi}_k > 0$ for any k , or $\tilde{w}_{m, n} > 0$ for any (m, n) , $\exists \tilde{a}_{\text{opt}} \in \mathbb{T}_+(M, N, K)$ such that $C(\tilde{a}_{\text{opt}}) = \inf_{\tilde{a} \in \mathbb{T}(M, N, K)} C(\tilde{a})$, i.e. (24) has a minimizer.

The extension of Lemma 6 to function spaces is challenging even in the case in which $\lambda > 0$ and $\xi(\sigma) > 0$ a.e. in $[0, \sigma_{\text{max}}]$. Even if it was possible to extract closed and bounded sublevel sets from the behavior of the regularizer, the characterization of compact sets in L^p involves L^p -equicontinuity, which does not seem to follow easily for our problem set-up. Nonetheless, the case $p = 2$ is slightly more tractable [53], and the possibility remains that the smoothing property of the kernels that compose the diffusion operator A can somehow be exploited. In any case, further characterizing the diffusion operator A , its range, nullspace and spectrum would surely help in addressing this issue and understanding its specifics. Uniqueness statements are challenging to obtain for both the continuous and discrete formulations. However, the intuition remains that, by coupling the third dimension with the non-negative group-sparsity regularizer, the optimization does not only get biased towards more plausible explanations of the data in terms of stationary sources, but the inverse problem also improves its condition by treating differently different $a \in \mathcal{A}_+$ that approximate the observation at the same level of accuracy $\|Aa - d_{\text{obs}}\|_{\mathcal{D}}$.

V. EXAMPLE ON REAL DATA AND CLOSING REMARKS

A. Example on real data

In Part II of this paper [13] we provide, along with the algorithmic developments, an extensive quantitative assessment of the proposed SL methodology. However, in order to keep this Part I self contained and exhibit the benefits of the contributed modeling and inverse problems framework, we analyzed a real Fluorospot image and compared the results to expert human labeling. In particular, we discretized an algorithm to solve (13) with $\lambda = 4000$, using $K = 6$ and $\{\tilde{\sigma}_0, \tilde{\sigma}_1, \dots, \tilde{\sigma}_6\} = \{2, 15, 20, 30, 40, 50, 70\}$. The details and approximations in the algorithmic solution were analogous to those used in the numerical results of Part II [13, Section III]. This resulted in a discretized recovered PSDR \tilde{a}_{opt} that, after minor post-processing (see Part II [13, Section III]) yielded an F1-Score relative to the human labeling of 0.9, with precision 0.92 and recall 0.88. A visualization of the image and some of the SL results are shown in Fig. 4. In terms of the cell count, our algorithm obtained 346 cell locations, while the human labeling contained 360 locations.

This image was obtained from a biochemical assay in which FITC dye was used as a marker, and it was captured

by an RGB sensor that produced raw data with dimensions $M = N = 2048$ and a dynamic range of $[0, 2^{16} - 1]$. This raw data was subject to a Bayer color filter array [54], in which neighboring pixels correspond to different color bands. Because the different color filters have different sensitivities to the particular wavelength emitted by the FITC molecules, neighboring pixels were weighted accordingly to estimate the underlying luminosity. The weighting function $\tilde{w}(\tilde{\mathbf{r}})$ was also updated to weight the errors in each position with respect to the sensor's sensitivity in that position. Additionally, the area comprised by the well was selected manually, and any position outside it was given weight zero, i.e. $\tilde{w}(\tilde{\mathbf{r}}) = 0$. Finally, the mask function $\mu(\tilde{\mathbf{r}})$ was set to 1 for all $\tilde{\mathbf{r}} \in \mathbb{Z}^2$.

In our opinion, the SL results produced by our algorithm are of a quality comparable to that of the expert human labeling. Indeed, in many cases the recovered location seems to be more reliable, and the criteria to determine what constitutes a true detection seems to be more consistent throughout the image.

B. Closing remarks

In this first part of our paper, we have developed a novel observation model for images that measure 3D reaction-diffusion-adsorption-desorption physical processes. This model provides an objective means to generate reliable synthetic data for biochemical assays from the specific physical parameters that characterize them. We have then proposed an optimization framework to recover reaction, i.e. particle secretion, by exploiting the assumption that it was spatially localized and temporally continuous. These properties are common in the context of SL in diffusion models, and are easy to interpret from the perspective of biochemical assays. Moreover, the designed optimization framework allows for the inclusion of different kinds of prior information, which can impact practical use greatly. To finalize the paper, we have introduced a simple discretization scheme to implement both synthesis and analysis methods based on our model, and we have provided some experimental results on real Fluorospot data.

In Part II of our paper [13], we develop an accelerated proximal gradient algorithm to solve the functional optimization problem in (13), providing an expression for the proximal operator of the non-negative group-sparsity regularizer. We also use the discretization scheme we presented here to derive an efficient implementation that approximates solutions of (24). Finally, we provide thorough empirical evaluation of our algorithm both in terms of detection and in terms of optimal transport metrics.

APPENDIX A

CHARACTERIZATION OF THE MODEL FROM PHYSICAL PARAMETERS

As in Section II-B, we will interchangeably rely on macroscopic arguments pertaining to the evolution of particle distributions, governed by (1), and microscopic arguments pertaining to the behavior of individual particles [44]. We start by presenting the proof of the characterization of the model in a simplified case, i.e., $\kappa_d = 0$.

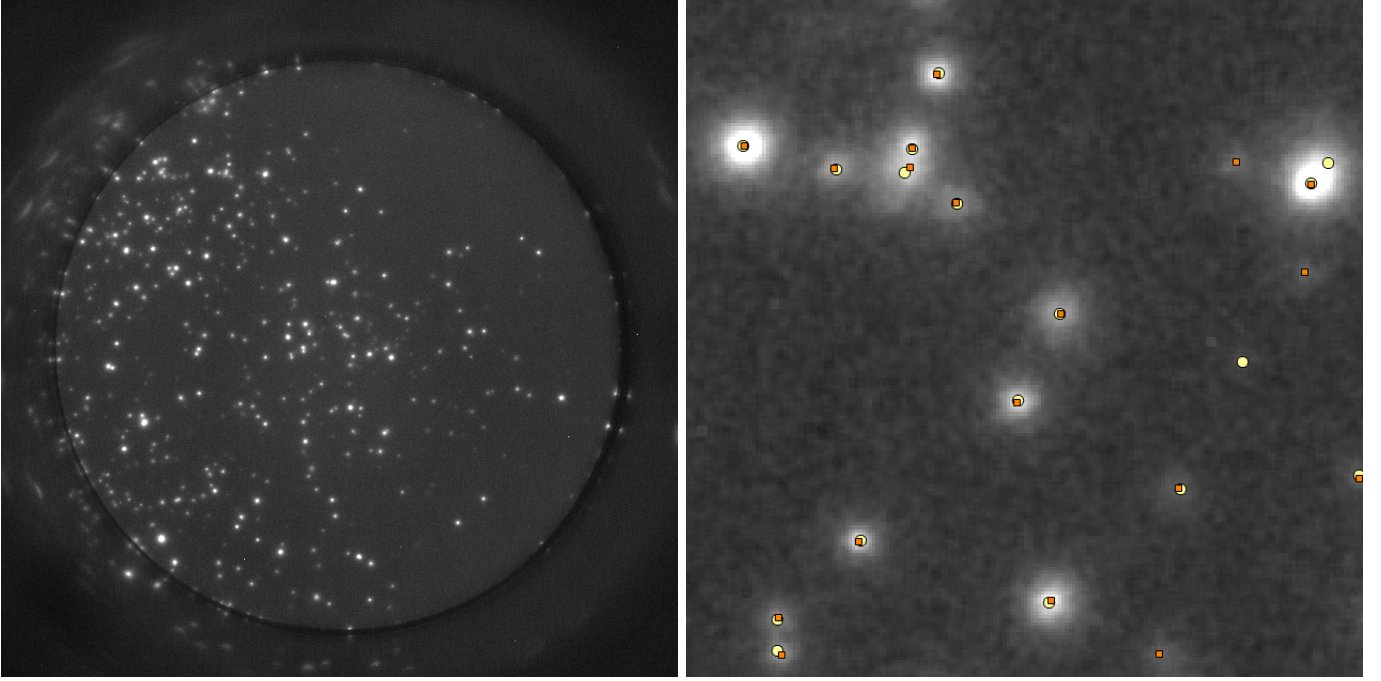


Fig. 4. Example of SL performance on a section of real Fluorospot data. To the left, grayscale image recovered from the raw RGB data, with increased luminosity. To the right, detection results (yellow circles) and human labeling (orange squares) for a specific section displayed on top of the grayscale image with increased luminosity.

Proof - Lemma 1 (Characterization of the observation model from physical parameters, Case $\kappa_d = 0$): From [55, Equation (3.1)] or [43, Equations (10), (22) and (27)] we have that, particles released at time 0 are, at time t , distributed in the z -dimension according to the density

$$u(z, t) = \frac{1}{\sqrt{\pi Dt}} \exp\left(-\frac{z^2}{4Dt}\right) - \frac{\kappa_a}{D} \exp\left(\frac{\kappa_a z + \kappa_a^2 t}{D}\right) \operatorname{erfc}\left(\frac{z}{\sqrt{4Dt}} + \kappa_a \sqrt{\frac{t}{D}}\right),$$

for $z \geq 0$. For $\kappa_d = 0$, bound particles are never released. Thus, the time until the first binding event is the same as the total time in free motion. For a particle released at time 0, the probability density function of the time until the first binding event is [3] $\phi(\tau) = \kappa_a u(0, \tau)$. Because τ was defined as the total time in free motion within the time window $[0, t)$, we have that $\varphi(\tau, t) = \phi(\tau) i_{[0, t)}(\tau)$. ■

We now present how this result is extended to $\kappa_d \geq 0$.

Proof - Theorem 2 (Characterization of the observation model from physical parameters): Consider first that, for $\kappa_d = 0$, (9) particularizes to (8), and, thus, our statement is already proved in Lemma 1.

Consider then the case $\kappa_d > 0$. Then, for any given time window, a particle that at the end of that period is bound has some probability of having been bound and remained still thereafter; some probability of having been bound, disassociated, and then bound again; some probability of having been bound and disassociated twice, and then bound again, and so on. Note that we focus only on those particles that are found bound at the end of a specific period, as those are the ones modeled by $\varphi(\tau, t)$ and (6). For any $i \in \{1, 2, \dots\}$,

consider the random variables τ_i and η_i , that represent the time spent in free motion and bound, respectively, the i -th time a particle goes through this cycle. The time invariance of (1), i.e., the lack of memory in the diffusion, association and disassociation processes, yields that $\{\tau_i\}_{i=1}^{\infty}$ and $\{\eta_i\}_{i=1}^{\infty}$ are mutually independent sequences of independent and equally distributed random variables.

Because both after release and after disassociation particles start their free motion at the surface, i.e. $z = 0$, the distribution of any specific τ_i is given by $\phi(\tau_i)$ as in (8), Lemma 1. Second, the probability density $\psi(\eta_i)$ of any η_i may be obtained from $\frac{\partial}{\partial \eta_i} \psi(\eta_i) = -\kappa_d \psi(\eta_i)$ [cf. (1b)] and $\int_{\eta=0}^{\infty} \psi(\eta_i) d\eta_i = 1$ as $\psi(\eta_i) = \kappa_d^{-1} e^{-\kappa_d \eta_i}$.

Consider now $\tau^{(j)}$, a random variable representing the total amount of time in free motion before the j -th disassociation event. Then, $\tau^{(j)} = \sum_{i=1}^j \tau_i$. Because $\tau_1, \tau_2, \dots, \tau_j$ are independent and identically distributed with density $\phi(\tau_i)$, the density of $\tau^{(j)}$ is given by the j -th convolutional power $\phi^{j*}(\tau^{(j)})$ of $\phi(\tau)$. Similarly, consider $\eta^{(j)}$, a random variable representing the total time a particle has been bound to the surface before the j -th disassociation event. Then, $\eta^{(j)} = \sum_{i=1}^j \eta_i$ and is distributed with density $\psi^{j*}(\eta^{(j)})$.

We now obtain the probability that a particle released at time 0 remains bound at time t , after having been bound a total of exactly j times, and having spent a total time $\tau = \tau^{(j)}$ in free motion. Note that this is equivalent to stating that $\eta^{(j)} \geq t - \tau^{(j)}$. Therefore,

$$\begin{aligned} \Pr(\tau = \tau^{(j)}) &= \Pr(\eta^{(j)} \geq t - \tau^{(j)}) = \int_{t - \tau^{(j)}}^{+\infty} \psi^{j*}(\eta) d\eta \\ &= p \left[j - 1; \kappa_d \left(t - \tau^{(j)} \right) \right], \end{aligned}$$

where $p[\cdot; \cdot]$ is the Poisson probability mass function as in (10). This result is naturally expected, as it merely states that the probability of the sum of the first j binding times exceeding $t - \tau^{(j)}$ is the same as the probability of having exactly $j - 1$ disassociation events during a time span of $t - \tau^{(j)}$. Indeed, at a disassociation rate of κ_d , this probability is given by the Poisson distribution with parameter $\lambda = \kappa_d (t - \tau^{(j)})$.

Using the law of total probability and that τ was defined as the time in free motion before time t only, we have that

$$\begin{aligned} \varphi(\tau, t) &= i_{[0,t)}(\tau) \sum_{j=1}^{\infty} \phi^{j*}(\tau) \Pr(\tau = \tau^{(j)}) \\ &= i_{[0,t)}(\tau) \sum_{j=1}^{\infty} \phi^{j*}(\tau) p[j-1; \kappa_d(t-\tau)]. \end{aligned}$$

■

Finally, we present the proof Lemma 2, that provides the truncation point of the infinite sum in Theorem 2 at which a certain accuracy $\epsilon > 0$ is guaranteed.

Proof - Lemma 2 (Truncation of the sum to characterize the model): Note first that, $\forall \lambda_1, \lambda_2 > 0$ such that $\lambda_1 > \lambda_2$, we have that $\sum_{j=J}^{+\infty} p[j, \lambda_1] > \sum_{j=J}^{+\infty} p[j, \lambda_2]$ for any $J \in \mathbb{N}$. Now, consider that, because $\phi(\tau)$ is a probability density defined for $\tau \in [0, +\infty)$, if we consider its extension by zeros, $\phi: \mathbb{R} \rightarrow \mathbb{R}_+$ such that $\phi(\tau) = 0$ for $\tau < 0$, we have that $\|\phi\|_{L^1(\mathbb{R})} = 1$. Then, using Young's inequality (see [56] for details), we have that $\|\phi^{(k+1)*}\|_{L^2(\mathbb{R})} \leq \|\phi^{k*}\|_{L^2(\mathbb{R})}$ for $k \geq 1$ and thus, $\|\phi^{k*}\|_{L^2(\mathbb{R})} \leq \|\phi\|_{L^2(\mathbb{R})} = \|\phi\|_{L^2(0,+\infty)}$ for any $k \geq 1$.

Using Young's inequality again [56] but with $r = \infty$, $p = q = 2$ and $n = 1$, we obtain that for any $f, g \in L^2(\mathbb{R})$, $\|f * g\|_{L^\infty(\mathbb{R})} \leq \|f\|_{L^2(\mathbb{R})} \|g\|_{L^2(\mathbb{R})}$.

Then, we have that for any $(\tau, t) \in [0, T]^2$ such that $\tau < T$,

$$\begin{aligned} \tilde{\varphi}(\tau, t) &= \sum_{j=J_\epsilon}^{+\infty} \phi^{j*}(\tau) p[j-1; \kappa_d(t-\tau)] \\ &\leq \sum_{j=J_\epsilon}^{+\infty} \|\phi^{j*}\|_{L^\infty(\mathbb{R})} p[j-1; \kappa_d(t-\tau)] \\ &\leq \sum_{j=J_\epsilon}^{+\infty} \|\phi\|_{L^2(\mathbb{R})} \|\phi^{(j-1)*}\|_{L^2(\mathbb{R})} p[j-1; \kappa_d(t-\tau)] \\ &\leq \|\phi\|_{L^2(0,+\infty)}^2 \sum_{j=J_\epsilon}^{+\infty} p[j-1; \kappa_d(t-\tau)] \\ &\leq \|\phi\|_{L^2(0,+\infty)}^2 \sum_{j=J_\epsilon}^{+\infty} p[j-1; \kappa_d T] \\ &\leq \|\phi\|_{L^2(0,+\infty)}^2 \frac{\epsilon}{\|\phi\|_{L^2(0,+\infty)}^2} = \epsilon. \end{aligned}$$

APPENDIX B

DIFFUSION AND INVERSE DIFFUSION

In this appendix, we present the proof to Lemmas 3 to 5, which characterize the diffusion operator A in Definition 5. Furthermore, we provide a proof of Lemma 6, that guarantees

the existence of a solution for the discretized version of the optimization problem that we propose for inverse diffusion.

Consider first Properties 1 and 2, which constitute a characterization of the Gaussian blur operators $\{G_\sigma\}_{\sigma>0}$ in Definition 2 in terms of their norm and adjoint operators.

Property 1 (Norm of the Gaussian blur operator). *The Gaussian blur operators in Definition 2 have norm 1, i.e.,*

$$\|G_\sigma\|_{\mathcal{L}(L^2(\mathbb{R}^2), L^2(\mathbb{R}^2))} = \|g_\sigma\|_{L^1(\mathbb{R}^2)} = 1.$$

Proof: For any $f \in L^2(\mathbb{R}^2)$, let $\check{f} \in L^2(\mathbb{R}^2)$ denote its Fourier transform. Then, we have that

$$\|f * g_\sigma\|_{L^2(\mathbb{R}^2)} = \|\check{f} \check{g}_\sigma\|_{L^2(\mathbb{R}^2)} \leq |\check{g}_\sigma(\mathbf{0})| \|\check{f}\|_{L^2(\mathbb{R}^2)} \quad (25a)$$

$$\begin{aligned} &= \int_{\mathbb{R}^2} g_\sigma(\boldsymbol{\rho}) d\boldsymbol{\rho} \|\check{f}\|_{L^2(\mathbb{R}^2)} \\ &= \|g_\sigma\|_{L^1(\mathbb{R}^2)} \|f\|_{L^2(\mathbb{R}^2)}. \end{aligned} \quad (25b)$$

In (25a), we have used the Parseval-Plancherel theorem and the convolution theorem followed by the bound on the Fourier transform of any real and non-negative function by the value at its origin. In (25b), we have used again the Parseval-Plancherel theorem, the expression for the Fourier transform evaluated at $\mathbf{0}$, and the non-negativity of the Gaussian kernel.

Consider now the sequence of Gaussian kernels with standard deviation $n \in \mathbb{N}$, i.e., $\{g_n\}_{n \in \mathbb{N}} \subset L^2(\mathbb{R}^2)$ and observe that $\|g_n\|_{L^2(\mathbb{R}^2)} = 1/(2\pi n)$. Further, $G_\sigma g_n = g_n * g_\sigma = g_{n+\sigma}$, and thus,

$$\frac{\|G_\sigma g_n\|_{L^2(\mathbb{R}^2)}}{\|g_n\|_{L^2(\mathbb{R}^2)}} = \frac{n}{\sigma + n} \rightarrow 1 \text{ when } n \rightarrow +\infty.$$

Therefore, (25) is tight and $\|G_\sigma\|_{\mathcal{L}(L^2(\mathbb{R}^2), L^2(\mathbb{R}^2))} = 1$. ■

Property 2 (Self-Adjointness of the Gaussian blur operator). *The Gaussian blur operators in Definition 2 are self-adjoint in $L^2(\mathbb{R}^2)$, i.e., $G_\sigma^* = G_\sigma, \forall \sigma > 0$.*

Proof: We will prove here that any convolutional operator from $L^2(\mathbb{R}^2)$ to $L^2(\mathbb{R}^2)$ with symmetric kernel is self-adjoint. This will yield the desired result because the Gaussian kernel in Definition 1 is symmetric. Let G be such an operator with symmetric kernel g . Recall the definition of adjoint from Section I-A. For any $f_1, f_2 \in L^2(\mathbb{R}^2)$, we have

$$\begin{aligned} (Gf_1 | f_2)_{L^2(\mathbb{R}^2)} &= \int_{\mathbb{R}^2} \int_{\mathbb{R}^2} g(\mathbf{r} - \boldsymbol{\rho}) f_1(\boldsymbol{\rho}) d\boldsymbol{\rho} f_2(\mathbf{r}) d\mathbf{r} \\ &= \int_{\mathbb{R}^2} \int_{\mathbb{R}^2} g(\boldsymbol{\rho} - \mathbf{r}) f_2(\mathbf{r}) d\mathbf{r} f_1(\boldsymbol{\rho}) d\boldsymbol{\rho} \\ &= (f_1 | Gf_2)_{L^2(\mathbb{R}^2)}, \end{aligned}$$

and thus $G^* = G$. ■

Properties 1 and 2 will now be used in the following two proof.

Proof - Lemma 3 (Boundedness of the diffusion operator): Recall that the norm of the operator A is defined as

$$\|A\|_{\mathcal{L}(\mathcal{A}, \mathcal{D})} = \sup_{a \in \mathcal{A}} \left\{ \frac{\|Aa\|_{\mathcal{D}}}{\|a\|_{\mathcal{A}}} \right\}.$$

Consider, then, that

$$\|Aa\|_{\mathcal{D}}^2 = \left\| w \int_0^{\sigma_{\max}} G_{\sigma} a_{\sigma} d\sigma \right\|_{L^2(\mathbb{R}^2)}^2 \quad (26a)$$

$$\leq \|w\|_{L^{\infty}(\mathbb{R}^2)}^2 \left\| \int_0^{\sigma_{\max}} G_{\sigma} a_{\sigma} d\sigma \right\|_{L^2(\mathbb{R}^2)}^2 \quad (26b)$$

$$= \eta^{-1} \sigma_{\max} \int_{\mathbb{R}^2} \left[\frac{1}{\sigma_{\max}} \int_0^{\sigma_{\max}} G_{\sigma} a_{\sigma} d\sigma \right]^2 d\mathbf{r} \quad (27a)$$

$$\leq \eta^{-1} \int_{\mathbb{R}^2} \int_0^{\sigma_{\max}} [G_{\sigma} a_{\sigma}]^2 d\sigma d\mathbf{r} \quad (27b)$$

$$= \eta^{-1} \int_0^{\sigma_{\max}} \|G_{\sigma} a_{\sigma}\|_{L^2(\mathbb{R}^2)}^2 d\sigma \quad (28a)$$

$$\leq \eta^{-1} \int_0^{\sigma_{\max}} \|a_{\sigma}\|_{L^2(\mathbb{R}^2)}^2 d\sigma = \eta^{-1} \|a\|_{\mathcal{A}}^2. \quad (28b)$$

Here, $\eta = \sigma_{\max}^{-1} \|w\|_{L^{\infty}(\mathbb{R}^2)}^{-2}$, (26) uses the fact that $w \in L^{\infty}(\mathbb{R}^2)$ to bound it by its maximum value, (27) uses Jensen's inequality on the convex function $\alpha \in \mathbb{R} \mapsto \alpha^2$, and (28) uses Property 1 to bound the norm of $G_{\sigma} a_{\sigma}$, $\forall \sigma > 0$. Therefore, $\forall a \in \mathcal{A}$, we have that

$$\frac{\|Aa\|_{\mathcal{D}}^2}{\|a\|_{\mathcal{A}}^2} \leq \sigma_{\max} \|w\|_{L^{\infty}(\mathbb{R}^2)}^2,$$

and, thus, $\|A\|_{\mathcal{L}(\mathcal{A}, \mathcal{D})} \leq \sqrt{\sigma_{\max}} \|w\|_{L^{\infty}(\mathbb{R}^2)}$. ■

Proof - Lemma 5 (Adjoint to the diffusion operator):

Recall the definition of adjoint from Section I-A. For any $a \in \mathcal{A}$, $d \in \mathcal{D}$, we have that

$$(Aa|d)_{\mathcal{D}} = \left(\left[\int_0^{\sigma_{\max}} G_{\sigma} a_{\sigma} d\sigma \right] | w^2 d \right)_{L^2(\mathbb{R}^2)} \quad (29a)$$

$$= \int_0^{\sigma_{\max}} (G_{\sigma} a_{\sigma} | w^2 d)_{L^2(\mathbb{R}^2)} d\sigma \quad (29b)$$

$$= \int_0^{\sigma_{\max}} (a_{\sigma} | G_{\sigma} \{w^2 d\})_{L^2(\mathbb{R}^2)} d\sigma \quad (29c)$$

$$= (a | d_s)_{L^2(\mathbb{R}^3)} = (a | \mu d_s)_{\mathcal{A}}. \quad (30)$$

Here, $d_s \in \mathcal{A}$ such that $d_s = G_{\sigma} \{w^2 d\}$, (29) uses the linearity of the integral and the inner product, and (30) uses that because $a \in \mathcal{A}$, $a(\mathbf{r}, \sigma) d_s(\mathbf{r}, \sigma) = 0$, $\forall \mathbf{r} \notin \text{supp}(\mu)$. Therefore, $A^* d = \mu d_s$. ■

We proceed by proving Lemma 4, which characterizes the nullspace of the diffusion operator in a simple but insightful way.

Proof - Lemma 4 (Nullspace of the diffusion operator):

Let $Aa = 0$. Then,

$$\begin{aligned} \int_{\mathbb{R}^2} (Aa)(\mathbf{r}) d\mathbf{r} &= \int_{\mathbb{R}^2} \int_0^{\sigma_{\max}} (G_{\sigma} a_{\sigma})(\mathbf{r}) d\sigma d\mathbf{r} \\ &= \int_{\mathbb{R}^2} \int_0^{\sigma_{\max}} \int_{\mathbb{R}^2} g_{\sigma}(\mathbf{r} - \boldsymbol{\rho}) a(\boldsymbol{\rho}, \sigma) d\boldsymbol{\rho} d\sigma d\mathbf{r} \\ &= \int_0^{\sigma_{\max}} \int_{\mathbb{R}^2} \int_{\mathbb{R}^2} g_{\sigma}(\mathbf{r} - \boldsymbol{\rho}) d\mathbf{r} a(\boldsymbol{\rho}, \sigma) d\boldsymbol{\rho} d\sigma \\ &= \int_0^{\sigma_{\max}} \int_{\mathbb{R}^2} a(\boldsymbol{\rho}, \sigma) d\boldsymbol{\rho} d\sigma \\ &= \|a_+\|_{L^1(\Omega)} - \|a_-\|_{L^1(\Omega)} = 0. \end{aligned}$$

We finalize this appendix by proving Lemma 6, which guarantees the existence of a minimizer of the non-negative group-sparsity regularized inverse diffusion problem under discretization.

Proof - Lemma 6 (Existence of a solution to the discretized problem): We will prove that $\forall \epsilon > 0$, $\exists \delta > 0$ such that $C(\tilde{a}) \leq \epsilon$ implies $\|\tilde{a}\|_2 \leq \delta$, i.e., $\tilde{a} \in \bar{\mathcal{B}}_{\delta} = \{\tilde{a} \in \mathbb{T}(M, N, K) : \|\tilde{a}\|_2 \leq \delta\}$. As a consequence, we will have shown that (24) is equivalent to

$$\min_{\tilde{a} \in [\bar{\mathcal{B}}_{\delta}]_+} \left\{ \left\| \tilde{A}\tilde{a} - \tilde{d}_{\text{obs}} \right\|_{\tilde{w}}^2 + \lambda \sum_{m,n} \left\| \tilde{\xi} \odot \tilde{a}_{m,n} \right\|_2 \right\}. \quad (31)$$

Because (31) is a minimization problem of a continuous function on a closed bounded set, the extreme-value theorem guarantees that it has a minimizer, and thus, (24) has a minimizer too.

Consider first the simpler case $\tilde{\xi}_k > 0$ for any $k \in \{1, 2, \dots, K\}$ and $\lambda > 0$. Then, for any $\epsilon > 0$, we have that $C(\tilde{a}) \leq \epsilon$ implies $f(\tilde{a}) \leq \epsilon$, which, for any (m, n) implies that $\left\| \tilde{\xi} \odot \tilde{a}_{m,n} \right\|_2 \leq \epsilon/\lambda$. Then, $\|\tilde{a}_{m,n}\|_2 \leq \epsilon/(\lambda \min_k \tilde{\xi}_k)$ for any (m, n) and

$$\|\tilde{a}\|_2 = \sqrt{\sum_{m,n} \|\tilde{a}_{m,n}\|_2^2} \leq \sqrt{MN} \frac{\epsilon}{\lambda \min_k \tilde{\xi}_k} = \delta.$$

Consider now the case in which either $\tilde{\xi}_k = 0$ for some k or $\lambda = 0$. Consider the decomposition of \tilde{a} on three unique components, i.e., $\tilde{a} = \tilde{a}_{\perp} + \tilde{a}_+ + \tilde{a}_-$, where \tilde{a}_{\perp} is the component on the orthogonal complement to the nullspace of \tilde{A} , while \tilde{a}_+ and \tilde{a}_- are the non-negative and non-positive parts of the component in the nullspace of \tilde{A} , i.e.,

$$\tilde{a}_{\perp} \in \mathcal{N}(\tilde{A})^{\perp} \quad \text{and} \quad \tilde{a}_N = \tilde{a}_+ + \tilde{a}_- \in \mathcal{N}(\tilde{A}).$$

Then, we have that if $\epsilon \geq C(\tilde{a})$, then

$$\begin{aligned} \sqrt{\epsilon} &\geq \left\| \tilde{A}\tilde{a} - \tilde{d}_{\text{obs}} \right\|_{\tilde{w}} \geq \left\| \tilde{A}\tilde{a}_{\perp} \right\|_{\tilde{w}} - \left\| \tilde{d}_{\text{obs}} \right\|_{\tilde{w}} \\ &= \left\| \tilde{w} \odot \tilde{A}\tilde{a}_{\perp} \right\|_2 - \left\| \tilde{d}_{\text{obs}} \right\|_{\tilde{w}} \\ &\geq \min_{m,n} \tilde{w}_{m,n} \left\| \tilde{A}\tilde{a}_{\perp} \right\|_2 - \left\| \tilde{d}_{\text{obs}} \right\|_{\tilde{w}} \\ &\geq \kappa \min_{m,n} \tilde{w}_{m,n} \|\tilde{a}_{\perp}\|_2 - \left\| \tilde{d}_{\text{obs}} \right\|_{\tilde{w}}, \end{aligned}$$

where κ is the smallest non-zero singular value of \tilde{A} , and, in conclusion,

$$\|\tilde{a}_{\perp}\|_2 \leq \frac{\sqrt{\epsilon} + \left\| \tilde{d}_{\text{obs}} \right\|_{\tilde{w}}}{\kappa \min_{m,n} \tilde{w}_{m,n}} = \delta_1.$$

Moreover, because $C(\tilde{a}) < +\infty$, the non-negative constraint must be satisfied, and therefore, $\|\tilde{a}_-\|_{\infty} \leq \|\tilde{a}_{\perp}\|_{\infty}$. Further, because $\mathbb{T}(M, N, K)$ is a finite-dimensional space, for any $p, q \in [1, \infty]$, $\exists c_{p,q} \geq 0$ such that for any $\tilde{a} \in \mathbb{T}(M, N, K)$, $\|\tilde{a}\|_p \leq c_{p,q} \|\tilde{a}\|_q$. Then, Lemma 4 yields that

$$\begin{aligned} \|\tilde{a}_N\|_2 &\leq c_{2,1} \|\tilde{a}_N\|_1 = 2c_{2,1} \|\tilde{a}_-\|_1 \\ &\leq 2c_{2,1} c_{1,\infty} \|\tilde{a}_-\|_{\infty} \leq 2c_{2,1} c_{1,\infty} \|\tilde{a}_{\perp}\|_{\infty} \\ &\leq 2c_{2,1} c_{1,\infty} c_{\infty,2} \|\tilde{a}_{\perp}\|_2, \end{aligned}$$

■

and

$$\begin{aligned} \|\tilde{a}\| &= \sqrt{\|\tilde{a}_N\|_2^2 + \|\tilde{a}_\perp\|_2^2} \\ &\leq \delta_1 \sqrt{1 + 4[c_{2,1}c_{1,\infty}c_{\infty,2}]^2} = \delta. \end{aligned}$$

ACKNOWLEDGMENTS

Doctor Holger Kohr, Axel Ringh and Assistant Professor Johan Karlsson provided valuable advice on operator discretizations. Professor Lars Jonsson provided valuable insights and helpful discussions on the solutions of (1). Doctor Christian Smedman provided expert labeling of the real Fluorospot data provided by Mabtech AB. The excellent team of anonymous reviewers provided feedback that improved the presentation of our results considerably. Of particular relevance were their pointing to the question of the existence of a solution to (13) and their suggestion of simpler proof techniques for Property 1.

REFERENCES

- [1] B. C. Lagerholm and N. L. Thompson, "Theory for ligand rebinding at cell membrane surfaces," *Biophysical Journal*, vol. 74, no. 3, pp. 1215–1228, 1998.
- [2] A. M. Lieto, B. C. Lagerholm, and N. L. Thompson, "Lateral diffusion from ligand dissociation and rebinding at surfaces," *Langmuir*, vol. 19, no. 5, pp. 1782–1787, 2003.
- [3] A. M. Berezhkovskii, L. Batsilas, and S. Y. Shvartsman, "Ligand trapping in epithelial layers and cell cultures," *Biophysical Chemistry*, vol. 107, no. 3, pp. 221–227, 2004.
- [4] I. Plante and F. A. Cucinotta, "Model of the initiation of signal transduction by ligands in a cell culture: Simulation of molecules near a plane membrane comprising receptors," *Phys. Rev. E*, vol. 84, p. 051920, Nov. 2011.
- [5] A. Y. Karulin and P. V. Lehmann, *Handbook of ELISPOT: Methods and protocols*, 2nd ed. Springer New York, 2012, ch. 11, pp. 125–143.
- [6] I. Plante and F. A. Cucinotta, *Theory and applications of Monte Carlo simulations*. InTech, 2013, ch. Monte-Carlo simulation of particle diffusion in various geometries and application to chemistry and biology, pp. 193–225.
- [7] C. C. Czerkinsky, L. Åke Nilsson, H. Nygren, Örjan Ouchterlony, and A. Tarkowski, "A solid-phase enzyme-linked immunospot (ELISPOT) assay for enumeration of specific antibody-secreting cells," *Journal of Immunological Methods*, vol. 65, no. 1, pp. 109–121, 1983.
- [8] A. Gazagne, E. Claret, J. Wijdenes, H. Yssel, F. Bousquet, E. Levy, P. Vielh, F. Scotte, T. L. Goupil, W. H. Fridman, and E. Tartour, "A Fluorospot assay to detect single T lymphocytes simultaneously producing multiple cytokines," *Journal of Immunological Methods*, vol. 283, no. 1–2, pp. 91–98, 2003.
- [9] T. Dillenbeck, E. Gelius, J. Fohlstedt, and N. Ahlberg, "Triple cytokine Fluorospot analysis of human antigen-specific IFN- γ , IL-17A and IL-22 responses," *Cells*, vol. 3, no. 4, pp. 1116–1130, Nov. 2014.
- [10] P. Martinez-Murillo, L. Pramanik, C. Sundling, K. Hultenby, P. Wretenberg, M. Spångberg, and G. B. Karlsson Hedestam, "CD38 and CD31 double-positive cells comprise the functional antibody-secreting plasma cell compartment in primate bone marrow," *Frontiers in Immunology*, vol. 7, p. 242, Jun. 2016.
- [11] T. Meier, H.-P. Eulenbruch, P. Wrighton-Smith, G. Enders, and T. Regnath, "Sensitivity of a new commercial enzyme-linked immunospot assay (T spot-tb) for diagnosis of tuberculosis in clinical practice," *European Journal of Clinical Microbiology and Infectious Diseases*, vol. 24, no. 8, pp. 529–536, 2005.
- [12] "High-throughput detection method for human papilloma virus (HPV) neutralizing antibodies," China Patent 104 880 555 A, Sep., 2015, cN Patent App. CN 201,510,346,407.
- [13] P. del Aguila Pla and J. Jaldén, "Cell detection by functional inverse diffusion and non-negative group sparsity—Part II: Proximal optimization and Performance evaluation," *IEEE Transactions on Signal Processing*, vol. 66, no. 20, Oct. 2018, available at: arXiv:1710.01622.
- [14] J.-C. Olivo-Marin, "Extraction of spots in biological images using multiscale products," *Pattern Recognition*, vol. 35, no. 9, pp. 1989–1996, 2002.
- [15] J. A. Rebhahn, C. Bishop, A. A. Divekar, K. Jimenez-Garcia, J. J. Kobia, F. E.-H. Lee, G. M. Maupin, J. E. Snyder-Cappione, D. M. Zaiss, and T. R. Mosmann, "Automated analysis of two- and three-color fluorescent ELISPOT (Fluorospot) assays for cytokine secretion," *Computer Methods and Programs in Biomedicine*, vol. 92, no. 1, pp. 54–65, 2008.
- [16] K. Pan, A. Kokaram, J. Hillebrand, and M. Ramaswami, "Gaussian mixture models for spots in microscopy using a new split/merge EM algorithm," in *IEEE International Conference on Image Processing (ICIP)*, Sep. 2010, pp. 3645–3648.
- [17] I. Smal, M. Loog, W. Niessen, and E. Meijering, "Quantitative comparison of spot detection methods in fluorescence microscopy," *IEEE Transactions on Medical Imaging*, vol. 29, no. 2, pp. 282–301, Feb. 2010.
- [18] Y. Kimori, N. Baba, and N. Morone, "Extended morphological processing: A practical method for automatic spot detection of biological markers from microscopic images," *BMC Bioinformatics*, vol. 11, no. 373, 2010.
- [19] S. Ram, J. J. Rodríguez, and G. Bosco, "Segmentation and detection of fluorescent 3D spots," *Cytometry Part A*, vol. 81A, no. 3, pp. 198–212, 2012.
- [20] J. Zhao, Y. Li, and S. Du, "A 3-D deconvolution based particle detection method for wide-field microscopy image," in *8th International Symposium on Medical Information and Communication Technology (ISMICT)*, Apr. 2014, pp. 1–5.
- [21] A. Basset, J. Boulanger, J. Salamero, P. Bouthemy, and C. Kervrann, "Adaptive spot detection with optimal scale selection in fluorescence microscopy images," *IEEE Transactions on Image Processing*, vol. 24, no. 11, pp. 4512–4527, Nov. 2015.
- [22] C. Kervrann, C. O. S. Sorzano, S. T. Acton, J. C. Olivo-Marin, and M. Unser, "A guided tour of selected image processing and analysis methods for fluorescence and electron microscopy," *IEEE Journal of Selected Topics in Signal Processing*, vol. 10, no. 1, pp. 6–30, Feb. 2016.
- [23] J. L. Starck, E. Pantin, and F. Murtagh, "Deconvolution in astronomy: A review," *Publications of the Astronomical Society of the Pacific*, vol. 114, no. 800, pp. 1051–1069, Oct. 2002.
- [24] Giovannelli, J.-F. and Coulais, A., "Positive deconvolution for superimposed extended source and point sources," *A&A*, vol. 439, no. 1, pp. 401–412, 2005.
- [25] K. Ehrenfried and L. Koop, "A comparison of iterative deconvolution algorithms for the mapping of acoustic sources," *AIAA Journal*, vol. 45, no. 7, pp. 1584–1595, Jul. 2006.
- [26] D. Marković, F. Antonacci, A. Sarti, and S. Tubaro, "Resolution issues in soundfield imaging: A multiresolution approach to multiple source localization," in *Applications of Signal Processing to Audio and Acoustics (WASPAA)*, 2015 *IEEE Workshop on*, Oct. 2015, pp. 1–5.
- [27] F. Ternat, P. Daripa, and O. Orellana, "On an inverse problem: Recovery of non-smooth solutions to backward heat equation," *Applied Mathematical Modelling*, vol. 36, no. 9, pp. 4003–4019, 2012.
- [28] W. Zhang, F. Ma, and Y. Sun, "The homotopy method for identifying the radiative source term in the heat conduction problem," *Applicable Analysis*, vol. 95, no. 4, pp. 842–859, 2016.
- [29] J. Matthes, L. Groll, and H. B. Keller, "Source localization by spatially distributed electronic noses for advection and diffusion," *IEEE Transactions on Signal Processing*, vol. 53, no. 5, pp. 1711–1719, May 2005.
- [30] A. Hamdi, "Identification of point sources in two-dimensional advection-diffusion-reaction equation: Application to pollution sources in a river. Stationary case," *Inverse Problems in Science and Engineering*, vol. 15, no. 8, pp. 855–870, 2007.
- [31] —, "Inverse source problem in a 2D linear evolution transport equation: Detection of pollution source," *Inverse Problems in Science and Engineering*, vol. 20, no. 3, pp. 401–421, 2012.
- [32] K. F. Kaarensen, "Deconvolution of sparse spike trains by iterated window maximization," *IEEE Transactions on Signal Processing*, vol. 45, no. 5, pp. 1173–1183, May 1997.
- [33] L. M. Li and T. P. Speed, "Deconvolution of sparse positive spikes," *Journal of Computational and Graphical Statistics*, vol. 13, no. 4, pp. 853–870, 2004.
- [34] V. Mazet, D. Brie, and C. Caironi, "Sparse spike train deconvolution using the Hunt filter and a thresholding method," *IEEE Signal Processing Letters*, vol. 11, no. 5, pp. 486–489, May 2004.
- [35] G. Kail, J. Y. Tournet, F. Hlawatsch, and N. Dobleigeon, "Blind deconvolution of sparse pulse sequences under a minimum distance constraint: A

- partially collapsed Gibbs sampler method,” *IEEE Transactions on Signal Processing*, vol. 60, no. 6, pp. 2727–2743, Jun. 2012.
- [36] I. W. Selesnick and I. Bayram, “Sparse signal estimation by maximally sparse convex optimization,” *IEEE Transactions on Signal Processing*, vol. 62, no. 5, pp. 1078–1092, Mar. 2014.
- [37] V. Duval and G. Peyré, “Exact support recovery for sparse spikes deconvolution,” *Foundations of Computational Mathematics*, vol. 15, no. 5, pp. 1315–1355, 2015.
- [38] C. Schwab and A. M. Stuart, “Sparse deterministic approximation of Bayesian inverse problems,” *Inverse Problems*, vol. 28, no. 4, p. 045003, 2012.
- [39] Z. Zhao and Z. Meng, “A modified Tikhonov regularization method for a backward heat equation,” *Inverse Problems in Science and Engineering*, vol. 19, no. 3, pp. 1175–1182, 2011.
- [40] Y. C. Hon and T. Takeuchi, “Discretized Tikhonov regularization by reproducing kernel Hilbert space for backward heat conduction problem,” *Advances in Computational Mathematics*, vol. 34, no. 2, pp. 167–183, 2011.
- [41] J. Wen, M. Yamamoto, and T. Wei, “Simultaneous determination of a time-dependent heat source and the initial temperature in an inverse heat conduction problem,” *Inverse Problems in Science and Engineering*, vol. 21, no. 3, pp. 485–499, 2013.
- [42] M. Reth, “Matching cellular dimensions with molecular sizes,” *Nature Immunology*, vol. 14, no. 8, pp. 765–767, Aug. 2013.
- [43] N. Agmon, “Diffusion with back reaction,” *The Journal of Chemical Physics*, vol. 81, no. 6, pp. 2811–2817, 1984.
- [44] T. S. Ursell, “The diffusion equation: A multi-dimensional tutorial,” California Institute of Technology, Pasadena, Tech. Rep., 2007.
- [45] P. Catala, V. Duval, and G. Peyré, “A low-rank approach to off-the-grid sparse deconvolution,” *Journal of Physics: Conference Series*, vol. 904, no. 1, p. 012015, 2017.
- [46] A. Tarantola, *Inverse problem theory and methods for model parameter estimation*. SIAM, 2005.
- [47] E. Zeidler, *Nonlinear functional analysis and its applications II/B. nonlinear monotone operators*. Springer Science+Business Media, LLC, 1990.
- [48] P. Mathé and S. V. Pereverzev, “Discretization strategy for linear ill-posed problems in variable Hilbert scales,” *Inverse Problems*, vol. 19, no. 6, p. 1263, 2003.
- [49] J. Kaipio and E. Somersalo, “Statistical inverse problems: discretization, model reduction and inverse crimes,” *Journal of Computational and Applied Mathematics*, vol. 198, no. 2, pp. 493–504, 2007, special Issue: Applied Computational Inverse Problems.
- [50] W. Erb and E. V. Semanova, “On adaptive discretization schemes for the solution of ill-posed problems with semiiterative methods,” *Applicable Analysis*, vol. 94, no. 10, pp. 2057–2076, 2015.
- [51] U. Hämarik, B. Kaltenbacher, U. Kangro, and E. Resmerita, “Regularization by discretization in Banach spaces,” *Inverse Problems*, vol. 32, no. 3, p. 035004, 2016.
- [52] D. B. Owen, “A table of normal integrals,” *Communications in Statistics - Simulation and Computation*, vol. 9, no. 4, pp. 389–419, 1980.
- [53] R. L. Pego, “Compactness in L_2 and the Fourier transform,” *Proceedings of the American Mathematical Society*, vol. 95, no. 2, pp. 252–254, 1985.
- [54] R. Lukac, *Single-sensor imaging: methods and applications for digital cameras*, 1st ed. Boca Raton, FL, USA: CRC Press, Inc., 2008.
- [55] A. Singer, Z. Schuss, A. Osipov, and D. Holcman, “Partially reflected diffusion,” *SIAM Journal on Appl. Math.*, vol. 68, no. 3, pp. 844–868, 2008.

- [56] W. Beckner, “Inequalities in Fourier analysis,” *Annals of Mathematics*, vol. 102, no. 1, pp. 159–182, 1975.



Pol del Aguila Pla (S’15) received a double degree in telecommunications and electrical engineering from the Universitat Politècnica de Catalunya, Barcelona, Spain, and the Royal Institute of Technology (KTH), Stockholm, Sweden, in 2014. Since August 2014, he is currently working toward the Ph.D. degree in electrical engineering and signal processing with KTH under the supervision of Joakim Jaldén. His Ph.D. work includes the research collaboration with Mabtech AB that led to the results published here and the development of the ELISPOT and Flourosport reader Mabtech IRISTM. Since August 2015, he is a Reviewer for the IEEE TRANSACTIONS ON SIGNAL PROCESSING. During 2017, he received a number of grants to support the international promotion of his research in inverse problems for scientific imaging, including a 2017 KTH Opportunities Fund scholarship, a Knut and Alice Wallenberg Jubilee appropriation, an Aforsk Foundation’s scholarship for travel and a 2017 Engineering Sciences grant from the Swedish Academy of Sciences (KVA, ES2017-0011).



Joakim Jaldén (S’03–M’08–SM’13) received the M.Sc. and Ph.D. degrees in electrical engineering from the Royal Institute of Technology (KTH), Stockholm, Sweden, in 2002 and 2007, respectively. From July 2007 to May 2009, he held a postdoctoral research position with the Vienna University of Technology, Vienna, Austria. He also studied at Stanford University, Stanford, CA, USA, from September 2000 to May 2002, and worked at ETH, Zurich, Switzerland, as a Visiting Researcher, from August to September, 2008. In July 2009, he returned to KTH, where he is currently a Professor of signal processing. His recent work includes work on signal processing for biomedical data analysis, and the automated tracking of (biological) cell migration and morphology in time-lapse microscopy in particular. Early work in this field was awarded a conference best paper Award at IEEE ISBI 2012, and subsequent work by the group has been awarded several Bitplane Awards in connection to the ISBI cell tracking challenges between 2013 and 2015. He was an Associate Editor for the IEEE COMMUNICATIONS LETTERS between 2009 and 2011, and an Associate Editor for the IEEE TRANSACTIONS ON SIGNAL PROCESSING between 2012 and 2016. Since 2013, he has been a member of the IEEE Signal Processing for Communications and Networking Technical Committee, where he is currently a Vice-Chair. Since 2016, he has also been responsible for the five year B.Sc and M.Sc. Degree Program in electrical engineering with KTH.

For his work on MIMO communications, he has been awarded the IEEE Signal Processing Societies 2006 Young Author Best Paper Award, the Distinguished Achievement Award of NEWCOM++ Network of Excellence in Telecommunications 2007–2011, and the best student conference paper Award at IEEE ICASSP 2007. He is also the recipient of the Ingvar Carlsson Career Award issued in 2009 by the Swedish Foundation for Strategic Research.